# PHASE RETRIEVAL USING ESTIMATION METHODS FOR INTENSITY CORRELATION IMAGING

A Thesis

by

BRIAN THOMAS YOUNG

Submitted to the Office of Graduate Studies of
Texas A&M University
in partial fulfillment of the requirements for the degree of

MASTER OF SCIENCE

August 2010

Major Subject: Aerospace Engineering

# PHASE RETRIEVAL USING ESTIMATION METHODS FOR INTENSITY CORRELATION IMAGING

A Thesis

by

BRIAN THOMAS YOUNG

Submitted to the Office of Graduate Studies of
Texas A&M University
in partial fulfillment of the requirements for the degree of

MASTER OF SCIENCE

Approved by:

| | |
|---|---|
| Chair of Committee, | David C. Hyland |
| Committee Members, | Torsten Siebert |
| | Srinivas Rao Vadali |
| Head of Department, | Dimitris Lagoudas |

August 2010

Major Subject: Aerospace Engineering

# ABSTRACT

Phase Retrieval Using Estimation Methods
for Intensity Correlation Imaging. (August 2010)
Brian Thomas Young, B.S., Texas A&M University
Chair of Advisory Committee: Dr. David C. Hyland

The angular resolution of an imaging system is sharply bounded by the diffraction limit, a fundamental property of electromagnetic radiation propagation. In order to increase resolution and see finer details of remote objects, the sizes of telescopes and cameras must be increased. As the size of the optics increase, practical problems and costs increase rapidly, making sparse aperture systems attractive for some cases. The method of Intensity Correlation Imaging (ICI) provides an alternative method of achieving high angular resolution that allows a system to be built with less stringent precision requirements, trading the mechanical complexity of a typical sparse aperture for increased computational requirements. Development of ICI has stagnated in the past due to the inadequacies of computational capabilities, but the continued development of computer technologies now allow us to approach the image reconstruction process in a new, more effective manner. This thesis uses estimation methodology and the concept of transverse phase diversity to explore the modern bounds on the uses of ICI.

Considering astronomical observations, the work moves beyond the traditional, single-parameter uses of ICI, and studies systems with many parameters and complex interactions. It is shown that ICI could allow significant new understanding of complex multi-star systems. Also considered are exoplanet and star-spot measurements; these are less promising due to noise considerations.

Looking at the Earth imaging problem, we find significant challenges, particu-

larly related to pointing requirements and the need for a large field-of-view. However, applying transverse phase diversity (TPD) measurements and a least-squares estimation methodology solves many of these problems and re-opens the possibility of applying ICI to the Earth-imaging problem. The thesis presents the TPD concept, demonstrates a sample design that takes advantage of the new development, and implements reconstruction techniques. While computational challenges remain, the concept is shown to be viable.

Ultimately the work presented demonstrates that modern developments greatly enhance the potential of ICI. However, challenges remain, particularly those related to noise levels.

TABLE OF CONTENTS

CHAPTER Page

I INTRODUCTION . . . . . 1

A. History and Development of the Hanbury Brown-Twiss Effect . . . . . 4
B. Fourier Optics and the Van Cittert-Zernike Theorem . . 8
C. System Definitions for an HBT-ICI Detector . . . . . 11
1. Derivation of the Hanbury Brown-Twiss Equations and Noise Components . . . . . 14
2. Phase Reconstruction . . . . . 17

II ASTRONOMICAL APPLICATIONS . . . . . 19

A. Historical Methods for Measuring Binary Separations and Stellar Radii . . . . . 19
B. Example: Tracking Multiple Star Systems . . . . . 23
1. Static Position Determination . . . . . 23
2. Dynamic Modeling and Estimation . . . . . 30
C. Other Potential Scenarios . . . . . 32
1. Star Spot Measurements . . . . . 33
2. Tracking Extra-solar Planets . . . . . 39

III EARTH IMAGING APPLICATIONS . . . . . 40

A. Focal Plane Design . . . . . 46
B. Phase Reconstruction Methods . . . . . 52
1. Conjugate Gradient Method and Analytical Gradients . . . . . 53
2. Results with Coarse Fourier Sampling . . . . . 56
C. Design Implications of Multi-Pixel Transverse Phase Diversity . . . . . 59
D. Sample System Design and Phase-Retrieval Simulation . 63
E. Conclusion . . . . . 69

IV CONCLUSION . . . . . 71

REFERENCES . . . . . 73

CHAPTER Page

APPENDIX A . . . . . 77

APPENDIX B . . . . . 79

VITA . . . . . 91

# LIST OF TABLES


| TABLE | | Page |
|---|---|---|
| I | Errors resulting from static multiple star position detections with varying SNR . . . . . | 28 |
| II | Comparison of static and dynamic estimation errors with SNR = 30 . | 32 |
| III | Integration times required for desired SNR in star-spot tracking . . . | 38 |
| IV | Statistics of TPD reconstruction with various pixel layouts . . . . . | 51 |
| V | Iterative steps of the conjugate gradient method . . . . . | 55 |

# LIST OF FIGURES


| FIGURE | | Page |
|---|---|---|
| 1 | NASA's Terrestrial Planet Finder (TPF), an example of a sparse, interferometric remote sensing platform . . . . . | 2 |
| 2 | The James Webb and Hubble space telescopes, examples of the two primary methods for maintaining optical quality precision . . . . | 3 |
| 3 | Circular rail used in the Narrabri intensity interferometer . . . . . | 5 |
| 4 | Optical reflectors used in the Narrabri intensity interferometer . . . . | 6 |
| 5 | Diffraction limited MTF of an ideal circular aperture . . . . . | 11 |
| 6 | Simple 3-aperture sparse system with associated MTF . . . . . | 12 |
| 7 | Block diagram of a typical intensity interferometer for astronomical observations . . . . . | 13 |
| 8 | Sample of coherence square magnitude values for binary separation measurements . . . . . | 20 |
| 9 | Mutual coherence square magnitude of stellar disks of varying radii . | 22 |
| 10 | Example star patterns and their coherence distributions . . . . . | 25 |
| 11 | Array layout and Fourier coverage for multiple star tracking . . . . . | 27 |
| 12 | Example cases for varying SNR study for multiple star positioning . | 29 |
| 13 | Coherence magnitude of a star model near the central spike . . . . . | 35 |
| 14 | Coherence magnitude of a star model far from the origin . . . . . | 37 |
| 15 | IKONOS commercial remote sensing satellite . . . . . | 41 |
| 16 | Sample illumination beam pattern for transverse phase diversity . . | 45 |

FIGURE Page

17 Footprint of a single detector in a diffraction limited system . . . . . 47

18 Example of a $3 \times 3$ TPD detector grid layout . . . . . 48

19 Example of super-pixel arrangements for comparison of convergence properties . . . . . 49

20 Reconstructed images for each of the super-pixel test cases, using the noise-free simulation . . . . . 50

21 Super-pixel layout and Fourier transform size for three examples used to test varying Fourier sampling rates . . . . . 56

22 Convergence of examples varying the Fourier sampling rate . . . . . 57

23 Reconstructed images for the three examples varying the Fourier sampling rate . . . . . 58

24 Sample image of Cape Canaveral used for considering coherence magnitude . . . . . 61

25 Dependence of the mean square mutual coherence value on the number of pixels in an image . . . . . 62

26 Physical aperture layout of example TPD-ICI system, overlaid on nominal full aperture . . . . . 64

27 Fourier plane coverage of example TPD-ICI system, overlaid on MTF of nominal full aperture . . . . . 65

28 Field of view and super-pixel size of example TPD-ICI system . . . . 66

29 Reconstructed image from simulated example TPD-ICI system . . . . 68

30 Meade LX200-GPS telescopes used for GAIA experiment . . . . . 81

31 SPMMini1020 avalanche photodiode assembly . . . . . 82

32 Rear-mounted devices on the telescope . . . . . 83

33 Pier-tech telescope shelter . . . . . 84

FIGURE Page

34 Telescope raising pier . . . . . 85

35 Pier-tech mobile telescope shelter . . . . . 86

36 Power systems for mobile observatory . . . . . 87

37 Pier-tech mobile telescope pier isolated from the trailer . . . . . 88

# CHAPTER I

## INTRODUCTION

Remote sensing of distant objects is the primary mission of many aeronautical and space systems. The volume of the instrument, and consequently its mass, both of which must be tightly budgeted in any aerospace application, are largely functions of the diameter of the aperture of the optical system. The size of the aperture is set by two parameters, the amount of light that one wishes to acquire to achieve a given signal quality, and the desired angular resolution of the system; a larger aperture allows more light to be gathered and focused onto the instruments, and also allows continuously finer details to be detected. While the only way to gather more light is to increase the area of the aperture, the angular resolution can be improved through the use of sparse telescopes and interferometric techniques. [1]

The fundamental limit of the angular resolution of an optical system is called the *diffraction limit*, resulting from the wave-like nature of photon propagation and interference [2]. As a wavefront travels from a distant source, it develops characteristic diffraction patterns that are related to the Fourier transform of the original image. If one were to capture all of these interference fringes and reverse the propagation direction, the original wavefront, and thus the original image, would be reproduced at the image plane. However, because only a subset of the fringes can be captured by any practical system, given that the aperture size must be finite, the system can only reproduce sufficiently large spatial frequencies of the image, and consequently cannot achieve a higher angular resolution than the diffraction limit.

Traditional methods for building sparse aperture systems involve placing reflec-

---

The journal model is *IEEE Transactions on Automatic Control.*

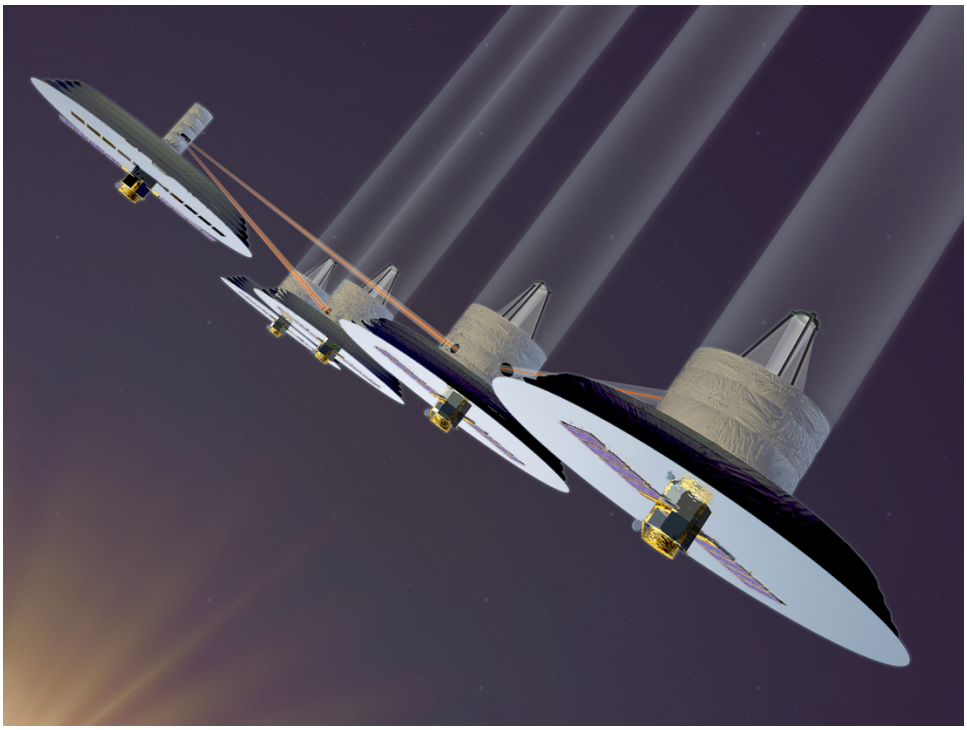

Fig. 1. NASA's Terrestrial Planet Finder (TPF), an example of a sparse, interferometric remote sensing platform

tive elements with very high precision (tens of nanometers) to act either as a sparse reflective telescope or as an interferometer. An interferometer explicitly measures the amount of interference between light at two points in space; a telescope reconstructs the image from this interference without explicitly measuring it. Both kinds of systems pose very difficult challenges due to the precision requirements, employing either complex active control systems or very stiff, heavy structural systems. The proposed NASA Terrestrial Planet Finder mission (TPF), shown in Figure 1, is a proposed interferometric, sparse aperture platform [3]. Though not sparse, NASA's James Webb and Hubble space telescopes (Figure 2) demonstrate how the system alignment must be maintained by either active controls or stiff, heavy, structures, respectively.

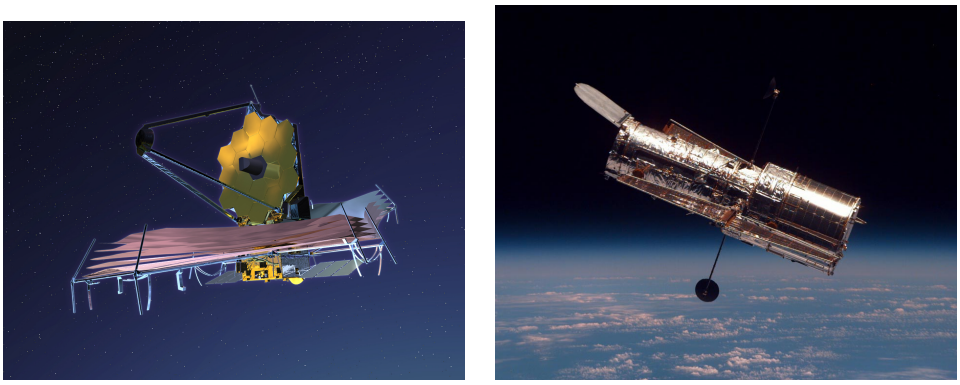

James Webb Space Telescope  Hubble Space Telescope

Fig. 2. The James Webb and Hubble space telescopes, examples of the two primary methods for maintaining optical quality precision

An alternative approach is known as Intensity Correlation Imaging (ICI), an interferometric method that measures the correlation between intensity fluctuations at two points in space, rather than measuring the interference patterns of the light waves themselves. This relies on the fact that all natural sources do not emit at an ideal monochromatic wavelength; instead the finite bandwidth of the light causes the light intensity to vary with unique *beat frequencies* as the multiple frequency components interfere with each other. These intensity modulations vary in a random and uncorrelated manner so that each element of the scene will vary its intensity in a uniquely identifiable manner, allowing interferometric correlation measurements. With low-bandwidth, quasi-monochromatic bands of light, these beat frequencies are many orders of magnitude slower than the frequency of the light itself, so that ICI requires much lower precision (typically millimeters or centimeters), in many cases does not require imaging-quality optics, and is largely unaffected by external disturbances caused by atmospheric variations (seeing) that limit many atmospheric

systems. It also allows all data to be transmitted and recorded in a purely digital format, facilitating multiple vehicle systems and the use of a very large number of baselines. All of this does come with disadvantages: the signal to noise ratio is fundamentally lower than other interferometric techniques, the field of view of the system is limited, and the loss of phase information introduces some ambiguities and requires a difficult phase-reconstruction processes.

### A. History and Development of the Hanbury Brown-Twiss Effect

The basis of ICI, intensity interferometry, was initially developed by Hanbury Brown in 1952 for use with radio astronomy [4]. However, because radio astronomy uses much longer wavelengths, direct measurement of the radio waves was and is a straightforward task, and the precision requirements were not so onerous; for radio astronomy, the disadvantages severely outweighed the advantages. Working with Twiss, however, they were able to show that the same effect could be measured at optical wavelengths, although there was some debate due to varying interpretations of quantum mechanics, the measurements of "photon bunching", and the self-interference of photons [5]. This quantum mechanical description is known as the Hanbury Brown-Twiss (HBT) effect.

The history of the use of HBT-based observations is unfortunately limited. The most prolific use of an intensity interferometer was carried out by Hanbury Brown, Davis and Allen at the Narribri observatory in the late 1960s. Their apparatus was used purely for stellar angular size measurements, using two 6.5 meter light collectors. These collectors were mounted on a circular rail track, pictured in Figure 3, to allow the measurements of the correlations at varying baselines up to 188 meters. In the center was a control building where the signals were collected.

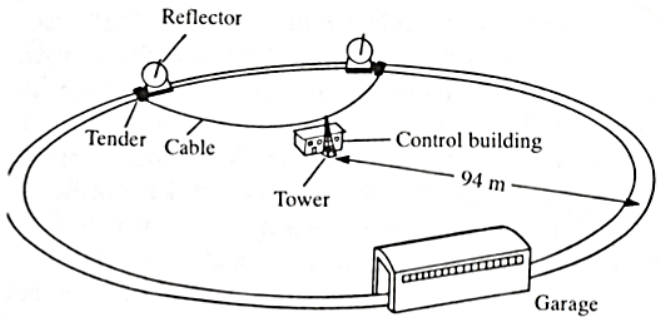


Fig. 3. Circular rail used in the Narrabri intensity interferometer

The reflectors themselves, shown in Figure 4 were constructed from 252 identical hexagonal mirrors, each constructed with the same focal length of 11 meters. The tolerance on the focal length of the segments was very low, within 15 cm, and their positions were arranged to simulate a paraboloidal surface as nearly as possible. The researchers first article details the construction and implementation of the device. [6]

Using this device, the astronomers measured and published the diameters of 32 stars. Due to the nature of the device, these stars were all fairly bright but small objects, which exemplified the advantages and disadvantages of ICI. Resolution of the sources required long baselines for which traditional interferometry was a difficult task, with the measurements ranging from 0.05 to 0.39 milliseconds of arc. However they were limited by signal quality, particularly with the electronics and sensor technology of the time, requiring the stars to be relatively bright, with magnitudes generally ranging from -1 to +1. A modern instrument could undoubtedly improve on these numbers, but metrology for single-baseline Michelson interferometers have also improved greatly, increasing the baseline distances greatly while maintaining their intrinsic sensitivity advantages.

Fig. 4. Optical reflectors used in the Narrabri intensity interferometer

The first observational interferometers were used by Michelson to measure the radius of astronomical objects. These more traditional instruments, *amplitude* interferometers, focus the light to a central location, where the visibility of the interference fringes are measured. This gives both the magnitude and phase of the mutual coherence function, and is a very powerful method for determining parameterized information such as stellar diameters. Because it requires the light beams to be of matched lengths down to a fraction of the wavelength (tens of nanometers for visible light), it can be a much more complex apparatus than an intensity interferometer. However, the signal quality is far superior, and the phase information is directly measurable.

While this is nearly always preferable for a single baseline system measuring a small number of parameters, the situation changes significantly when we consider attempts to retrieve a literal image, or any other situation with a large number of unknowns and a similarly large number of measurements. The construction requirements of an amplitude interferometer are no different than those for a sparse telescope, recommending to us that a sparse telescope is a better, simpler solution for most situations, since it eliminates the finite sampling of the Fourier field that limits the field of view (discussed more in Chapter III). Also, as more apertures are added to an amplitude interferometer, the light beams are split multiple times, reducing the signal quality of each individual measurement as more are taken. ICI, however, maintains the signal quality of each measurement by eliminating propagation degradation, since only digital data is passed beyond the original detector. As more measurements are taken, the signal to noise of the resulting reconstruction is increased, up to a limit placed on it by the total aperture size. This maintains the advantages of ICI over traditional imaging, and is much more expandable than an amplitude interferometer.

The primary reason for the lack of past implementation, and the renewed interest

in recent years is due to the acceleration of computer technology. In the past, the amount of calculation required to record, correlate and interpret the incoming light was far beyond the capabilities of analog systems with more than a few detectors, after which the phase would still need to be reconstructed. Digital computational capabilities have now increased to the point where it is reasonable to record and interpret the data, and process them with iterative techniques and least-squares solvers, in order to obtain an image in an acceptable time frame. The computational requirements of a given concept will still be a driving parameter, but it is now conceivable to do such a thing.

Ofir and Ribak offer a very enthusiastic review of a concept that uses linear arrays of large 100 meter reflectors that could be used to image extra-solar planets and resolve very high angular resolutions. [7, 8] However, many of their results are optimistic and the design of such an array, even with the crudeness of the optics, would still be a significant undertaking. Herrero studied array layouts that would yield the best coverage for an ICI system, making use of redundancies to improve SNR. [9] Hyland, with various students, including the author, has developed a number of space-borne concepts with varying levels of feasibility, particularly studying the aspects of spacecraft and constellation design. [10, 11, 12]

## B. Fourier Optics and the Van Cittert-Zernike Theorem

Fundamental to any kind of sparse aperture system are the concepts of Fourier optics, which provide an especially convenient and powerful interpretation of the wave propagation of light over long distances [13]. The van Cittert-Zernike theorem demonstrates that the cross-correlation or *mutual coherence* of the electromagnetic field at two points at a sufficient distance is proportional to the Fourier transform of the

intensity at the object plane, and thus what we interpret as an image of the object. In order to capture the desired details and perform the inverse transform, a sparse system must be capable of sufficiently sampling this Fourier field.

The mutual coherence is a measure of the similarity of the electromagnetic field at two points in space. Defining the complex field at a point $k$ as $V_k$, the mutual coherence of the field between points $i$ and $j$ is

$$\Gamma_{i,j} = \langle V_i^* V_j \rangle \,. \tag{1.1}$$

Using the Huygens-Fresnel principle, and given a field in the object plane from an incoherent source, the mutual coherence in the far field can be defined as

$$\Gamma_{i,j} = \frac{1}{R^2} \iint\limits_O \langle I(\rho) \rangle \exp[-2\pi i(\mathbf{x} \cdot \rho)] d^2\rho, \tag{1.2}$$

where

$$\mathbf{x} = \lambda^{-1}(\mathbf{r}_j - \mathbf{r}_i), \tag{1.3}$$

so that the mutual coherence function is, within a reasonable approximation, the Fourier transform of the image intensity. This is commonly known as the van Cittert-Zernike theorem. Note that the Fourier coordinate vector is proportional to the relative separation of the detectors, commonly called the *baseline*, rather than their absolute position. Thus, the separations between apertures are the relevant design parameter. In this formula, $R$ is the distance separating the origins of the detector coordinates and and object coordinates, $I$ is the object intensity, $O$ is the surface of the object, $\mathbf{r}$ are coordinates in the detector frame and $\rho$ are object coordinates. A derivation is given in appendix A.

Given the inherent reversibility of the Fourier transform, all image forming processes can be interpreted as methods for taking the inverse transform of the mutual

coherence. A traditional full-aperture telescope focuses the light onto the image plane, as is commonly shown with ray-based approximations. Treating two rays entering the aperture as an analog to Young's double slit experiment, each set of rays create an interference pattern with a period inversely proportional to the separation of their point of entry; a telescope recreates the image by using these interference patterns to reproduce every Fourier component of the image. Because it samples the Fourier space with infinite fineness, the total image size or field of view is only limited by physical obstacles and aberrations.

However, if the system is unable to capture some components of the the mutual coherence field, some details of the scene will not be detected. There are two forms of this phenomenon: the first is an upper limit on the highest spatial frequency detected, the diffraction limit, and the second is the existence of voids within the overall sampling region in the Fourier plane. The ability of an optical system to capture particular spatial frequencies is commonly expressed by the *modulation transfer function* (MTF) $\mu$. Given an aperture function $A$, for a diffraction limited system, the MTF can be calculated by taking the convolution of the aperture with itself. For a circular aperture with no blockage, this function takes the familiar conical form shown in Figure 5. The overall radius of the MTF is defined by the furthest separated parts of the aperture, scaled by the wavelength. That is, $r_{MTF} = D/\lambda$. A second method for constructing $\mu$, one which takes into account aberrations and errors not captured in pure Fourier optics, is that $\mu = \mathrm{FT}^{-1}(\psi)$, where $\psi$ is the point spread function of the optical system. With our form of non-traditional optics, though, the point spread function has no real physical meaning beyond being the transform of the MTF, making the first method of calculating it more applicable.

Now, we are concerned specifically with the performance of sparse aperture sys-

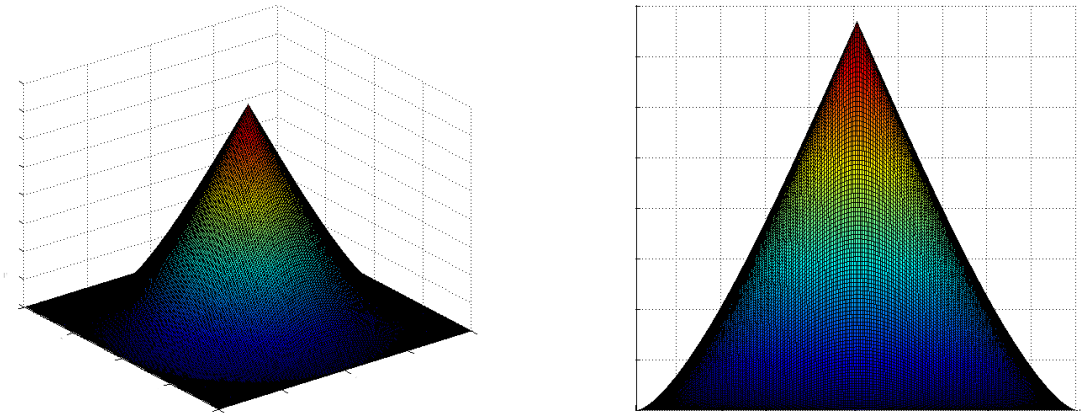

Fig. 5. Diffraction limited MTF of an ideal circular aperture

tems. The simplest system we can create uses three circular apertures arranged in an equilateral triangle, separated by a distance of $2D$. This arrangement, along with its MTF, is shown in Figure 6. The arrangement gives non-zero MTF coverage out to the radius of a full circular aperture of the same size, in a hexagonal pattern. However, the sparseness leaves areas of very low signal quality. By decreasing the distance between the apertures, these high-noise regions can be reduced. More complex arrangements such as the Golay arrays and computationally optimized designs can yield larger and sparser arrangements; Golay arrays will be used for sample designs in the following chapters [14].

## C. System Definitions for an HBT-ICI Detector

An intensity interferometer operates by measuring the intensity of the light from a source, and correlating the variations in the intensity. As shown in Figure 7, a typical intensity interferometer for astronomical observations consists of an optical system

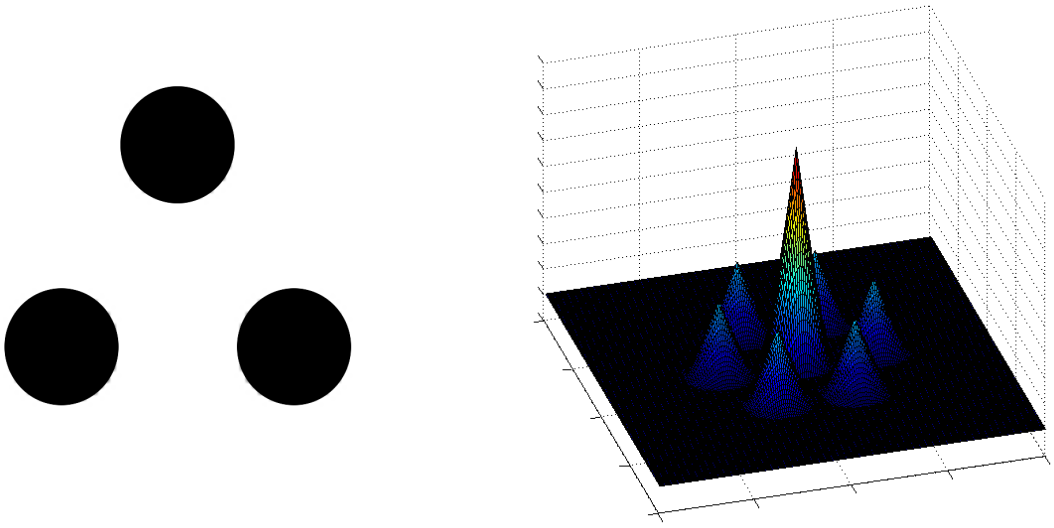

Aperture Modulation Transfer Function

Fig. 6. Simple 3-aperture sparse system with associated MTF

for focusing the light onto high-speed photo-detectors, from which the signals are passed into an electronics package. In the electronics package, a high-pass filter is applied to the signals from both detectors, so that only the variations in the intensity remain. After this, the signals are then cross-correlated by a signal multiplier. At this point the signal is proportional to the square magnitude of the mutual coherence field, which should be a constant or slowly varying value. A low-pass filter is applied to remove extraneous noise.

Unlike in most optical systems, the optical components of an ICI system are not explicitly required to form an image at their focus. Rather, the optical components have two purposes: to gather more light for the sensor, and to limit the field-of-view to the region of interest. The first, the gathering of more light, improves the signal quality and system performance, allowing more photons to be measured and

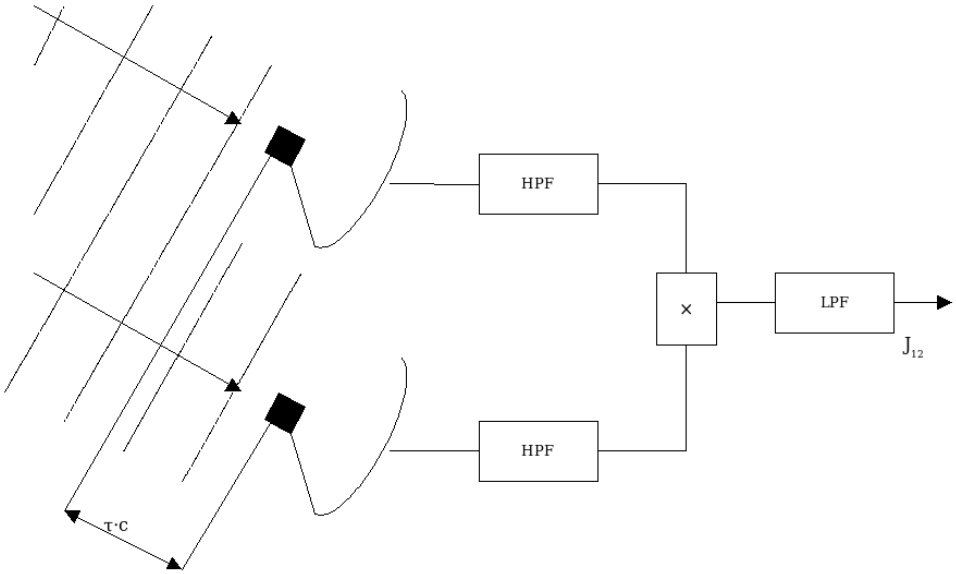


Fig. 7. Block diagram of a typical intensity interferometer for astronomical observations

the effects of read noise, photon (shot) noise, and other effects to be reduced. This is valuable in astronomy, although the effects advantages are tempered when observing a large-scale scene such as the Earth's surface, because the size of the scene (and thus the number of photons) must vary inversely with the aperture size. The second critical consideration is to prevent light from outside the desired region of interest to impact the detector surface; failure to do so will leave spurious signals that will overwhelm useful information in the signal. This is straightforward for an astronomical target, but is a much harsher requirement for a large, resolvable scene such as the Earth's surface.

Early astronomical instruments used by Hanbury Brown were incapable of forming an image. The first were constructed from surplus spotlight reflectors; the more advanced system at Narribri was constructed of better quality, but were still very low

quality compared to a true telescope. However, as will be discussed in more detail in Chapter III, an earth-looking system will necessarily require high-quality optics in order to limit the field of view, since the black of space does not surround the target. At an opposite extreme, if one were to attempt measurements of a sufficiently bright single target in an otherwise dark room, an optical system would be entirely unnecessary, since the bare detectors would be able to achieve the desired signal quality, and there would be no stray light to consider.

ICI specifically refers to an extension of the intensity interferometer concept. By using more than two detector assemblies (optical systems with high-speed detectors and high-pass filters), multiple mutual coherence measurements along multiple baselines are possible. If the Fourier field is sampled sufficiently, enough information can be gathered to allow the reconstruction of a literal image of the target.

### 1. Derivation of the Hanbury Brown-Twiss Equations and Noise Components

Now we consider the output $M$ of the intensity interferometer, taken over a long enough period that we can ignore quantum effects. We define the brackets $\langle \cdots \rangle$ as a time average over this period, so that it is equivalent to the expectation operator. In this system, where the output signal is proportional to the intensity by constant $\kappa$, the ideal output is

$$M_{1,2} = \kappa^2 \left\langle \left(I_1 - \langle I_1 \rangle\right) \left(I_2 - \langle I_2 \rangle\right) \right\rangle . \tag{1.4}$$

Carrying out the multiplication and recognizing the linearity of the $\langle \cdots \rangle$ operator, this becomes

$$\begin{aligned} M_{1,2} &= \kappa^2 \left( \langle I_1 I_2 \rangle - \langle I_1 \langle I_2 \rangle \rangle - \langle I_2 \langle I_1 \rangle \rangle + \langle I_1 \rangle \langle I_2 \rangle \right) \\ &= \kappa^2 \left( \langle I_1 I_2 \rangle - \langle I_1 \rangle \langle I_2 \rangle \right) . \end{aligned} \tag{1.5}$$

Now, we express the intensities in terms of their component electric fields $V_k$

$$I_k = V_k^* V_k. \tag{1.6}$$

Note that we assume a polarized field for clarity; however, the uncorrelated nature of the perpendicular field components will ultimately yield the same result for the unpolarized case. Equation (1.1) defines the mutual coherence function in terms of the electric field. Given these definitions, and the Gaussian moment theorem (recall that $\langle \cdots \rangle$ is equivalent to the expectation operator), we see that

$$\begin{aligned} \langle I_1 I_2 \rangle &= \langle V_1^* V_1 V_2^* V_2 \rangle \\ &= \langle V_1^* V_1 \rangle \langle V_2^* V_2 \rangle + \langle V_1^* V_2^* \rangle \langle V_1 V_2 \rangle + \langle V_1^* V_2 \rangle \langle V_1 V_2^* \rangle \\ &= \langle I_1 \rangle \langle I_2 \rangle + |\Gamma_{1,2}|^2 . \end{aligned} \tag{1.7}$$

Applying this to equation (1.5), the mean intensities are eliminated and

$$M_{1,2} = \kappa^2 |\Gamma_{1,2}|^2 . \tag{1.8}$$

Finally, we can extract the normalized coherence $\gamma$ as

$$|\gamma_{1,2}|^2 = \frac{M_{1,2}}{M_1 M_2} \tag{1.9}$$

where $M_k = \kappa I_k$ are the intensity outputs of the individual detectors.

A more complete derivation is available in reference [15]. The above derivation ignores the quantized nature of light, the effects of large apertures, the variations caused by varying integration times, and other components that we effectively encompass in the constant $\kappa$. Defining $\alpha$ as the quantum efficiency, $c$ as the speed of light, $T_c$ as the correlation time, $T_d$ as the detector response time, and $T_a$ is the averaging time, and $S_k$ as the $k$th aperture, then the final measured value is more

accurately

$$M_{1,2} = \frac{1}{2}\kappa^2\alpha^2c^2T_cT_d\left(1-\frac{2T_d}{T_a}\right)\int_{S_1}\int_{S_2}\langle I_1\rangle\langle I_2\rangle|\gamma|^2\,d^2\mathbf{x}_2\,d^2\mathbf{x}_1. \tag{1.10}$$

Here, the term $cT_c\langle I\rangle$ represents the mean number of photons per square meter, per second, per Hertz bandwidth. Note that this derivation depends on the assumption of a square wave as the impulse response of the photo-detector. However, because $T_d << T_a$ this does not make a significant difference in the final result.

The value in equation (1.10) is actually the ensemble average or first moment of the results over a finite averaging time. Because of the statistical nature of photon impacts on the detector, even a completely noiseless system will yield some uncertainty in the final result. This is called photon or shot noise. By determining the second moment of the statistical results, assuming a Gaussian distribution, the standard deviation can be evaluated, ultimately yielding a fundamental limit to the signal to noise ratio. Though the derivation is beyond the scope of this work, this fundamental limit is

$$SNR = \frac{\sqrt{\frac{3}{4}}\alpha cT_c\sqrt{\frac{T_a}{T_d}}\int_{S_1}\int_{S_2}\langle I_1\rangle\langle I_2\rangle|\gamma|^2\,d^2\mathbf{x}_2\,d^2\mathbf{x}_1}{\sqrt{\int_{S_1}\langle I_1\rangle\,d\mathbf{x}_1\int_{S_2}\langle I_2\rangle\,d\mathbf{x}_2}}. \tag{1.11}$$

Making the approximation that the intensities and mutual coherence are constant over the surface apertures, and equal apertures and intensities, this can be reduced to

$$SNR \approx \alpha cT_c\langle I\rangle S|\gamma|^2\sqrt{\frac{T_a}{T_d}}. \tag{1.12}$$

Note that the SNR is proportional to the value of the signal ($|\gamma|^2$), since the random photon noise does not vary with the mutual coherence. This is very important for the sizing of the imaging system for a large field of view system, since it implies that

the signal is limited by a constant magnitude noise floor.

Deviations from this approximation will reduce the signal quality (i.e. this is an upper limit), and will generally be increased as the size of the region of interest increases. As the size of the target increases, the regions of relatively constant intensity and coherence grow smaller: so that our removal of the integrals in equation (1.10) is more more invalid. This averaging over the apertures was recognized by Hanbury Brown and Twiss, described by them as the *partial coherence effect*. Generally, in order to maintain sufficient signal quality, the region of interest must be smaller than the ideal diffraction limited spot of the aperture.

## 2. Phase Reconstruction

Note that equations (1.8) and (1.10) only yield the magnitude of the mutual coherence, but not the complex phase information. However, information on the phase is necessary in order to successfully take the inverse transform and reconstruct the image. This problem, commonly called the *phase problem*, is faced in many fields, and there are many solutions.

Early methods for phase reconstruction involved iterative processes of supposing a solution for the phases, conforming that solution to known image constraints and altering the supposed phases by some formula to bring it closer to the constrained solution. Fienup did significant studies on these methods during the late 1970s and 1980s, although the origin of these methods is attributed to Gerchberg and Saxton a few years before Fienup. Further work has been done to extend the applications and provide better definition of constraints and requirements.

Fienup's experimentation with these methods led to the conclusion that these methods were effective for determining unique solutions with two-dimensional objects,

though one-dimensional objects would often converge to multiple unrelated solutions. Also, a combination of different terms for the constraint enforcement equation, when changed randomly as the system iterated, provided the best convergence. Finally, it was shown that the method converged more quickly given a good initial guess as to the solution. [16]

Note also that convergence is absolutely dependent on having at least 50% of the pixels in the image constrained to known values. Observing an astronomical object, this is straightforward, because the surrounding space will be well known as black. A second issue that occurs are ambiguities in the reconstruction. The process is not able to distinguish translations or rotations in the final image, because these are expressed as constant phase shifts, and only relative phase information can be determined. Both of these pose particular problems when considering an earth-looking system.

A more systematic approach is to consider phase reconstruction as a least-squares estimation process, where the known Fourier magnitudes are the measurements, and the image pixels or scene parameters are the states to be estimated. By approaching the problem in this manner, standard non-linear programming (NLP) approaches can be used. It also gives more insight into the pixel constraint requirement. Because the Fourier transform is symmetric, the full Fourier transform of an $N \times N$ image contains $N^2/2$ independent magnitude measurements, and as many independent phase measurements. Thus, in order to have a well posed problem without the phase information, only half of the image pixels can be unknown. If other solutions can be found to impose constraints or take more measurements, the more robust framework of an estimation approach can allow proper convergence of the solutions. Applying this least-squares approach is the primary focus of this thesis.

# CHAPTER II

## ASTRONOMICAL APPLICATIONS

As stated in the introduction, previous work using intensity interferometry has focused on observations of astronomical targets, as opposed to earth-imaging. This is because the targets are point sources, observations can be run continuously for hours, and there is no alternative to improve the observation environment. We will explore estimation methodology for parameter measurement in this context first, before expanding it to earth-imaging in the next chapter.

### A. Historical Methods for Measuring Binary Separations and Stellar Radii

Historically, Michelson interferometers were initially used to measure the separation distances of binary star systems [2]. Although the existence of these binaries were determined visually, by measuring the changes in the interference fringes as the Michelson apertures were moved, the actual angular separations were measured much more precisely. In order to measure these separations using intensity correlations, we approximate the stars as two delta functions, defining the scene $s$ as

$$s(x,y) = \alpha_0 \delta(x - x_0, y - y_0) + \alpha_1 \delta(x - x_1, y - y_1), \tag{2.1}$$

so that its mutual coherence, or visibility, is

$$\Gamma(u,v) = \alpha_0 \exp\left(-2\pi i(x_0 u + y_0 v)\right) + \alpha_1 \exp\left(-2\pi i(x_1 u + y_1 v)\right), \tag{2.2}$$

and the measured square magnitude is

$$M(u,v) = \alpha_0^2 + 2\alpha_0\alpha_1 \cos(2\pi i((x_1 - x_0)u + (y_1 - y_0)v)) + \alpha_1^2. \tag{2.3}$$

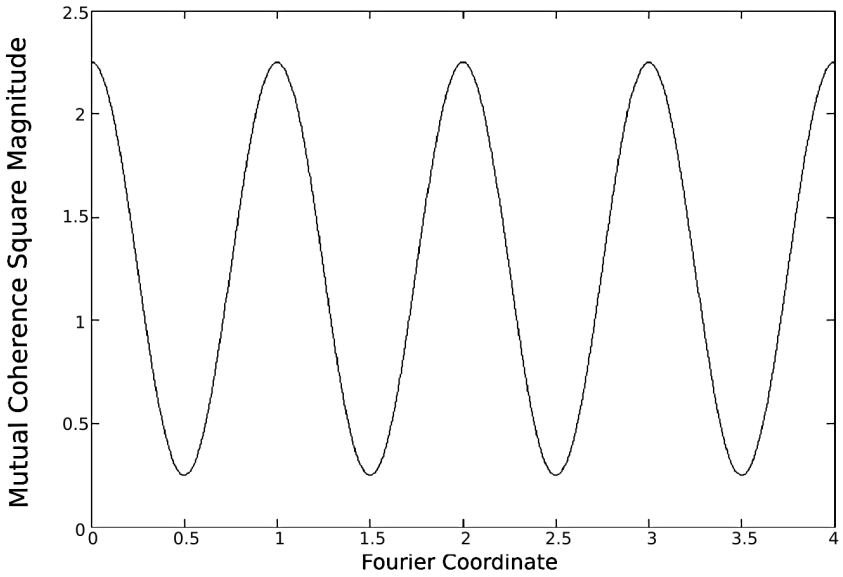


Fig. 8. Sample of coherence square magnitude values for binary separation measurements

Calculating this where $\alpha_0 = 1$, $\alpha_1 = 0.5$, the separation in the $x$ direction is 1 and there is no $y$ separation, the results are plotted along the $u$ direction in Figure 8. The mean measurement is equal to the sum of the squares of the magnitudes, while the difference between the stars magnitudes directly determines the magnitude of the sinusoidal variations. Finally, the separation distance determines the frequency of the variations; the direction can be determined by finding the direction with the lowest frequency. All of these measurements can thus be determined easily and independently given low-noise measurements.

Originally, intensity interferometry was used to measure the diameter of bright stars through curve fitting. By assuming a simple model of the star as a disk in the sky, the measurements at Fourier coordinates $(u, v)$, according to the model, are

easily determined as

$$\begin{aligned} |\Gamma(u,v)|^2 &= \left| \mathrm{FT}\left[ \alpha_0 \mathrm{circ}\left( \frac{\sqrt{x^2+y^2}}{r} \right) \right] \right|^2 \\ &= \alpha_0^2 r^2 \frac{J_1^2\left(2\pi r\sqrt{u^2+v^2}\right)}{u^2+v^2}, \end{aligned} \tag{2.4}$$

where the two parameters to be solved for are the stellar radius $r$, and the associated surface brightness $\alpha_0$. Figure 9 shows the profile of this function for $r = \frac{1}{2}, 1, 2$, to demonstrate how measurements of these functions, out to approximately $0.5r^{-1}$ in the Fourier coordinates can be used to effectively estimate stellar diameters. Considering a sun-sized star at 15 light-years, the apparent diameter from Earth would be $4.64 \times 10^{-9}$ radians. Thus, according to our rule above, an instrument capable of determining this radius would need to be $10^8\lambda$ across, or a maximum baseline of 50 meters for $\lambda = 500$ nm. Other components, such as starspots, planets, and limb darkening, may have some effect on the measurements; if taken within the prescribed radius, though, the perturbations caused by these will be significantly less than the noise in the system.

This kind of single-variable curve fitting (the magnitude of the star was normalized out of the measurement) was the limit of what was possible in the 1970s given the state of technology. With the limits in sensitivity, after the Narrabri observatory completed its study of the 32 brightest stars, further work on intensity interferometry ceased. However, the explosion in computer technology in the intervening years, and development of solution techniques for large multi-variable non-linear programming problems opens up new possibilities for estimating more complex scenes.

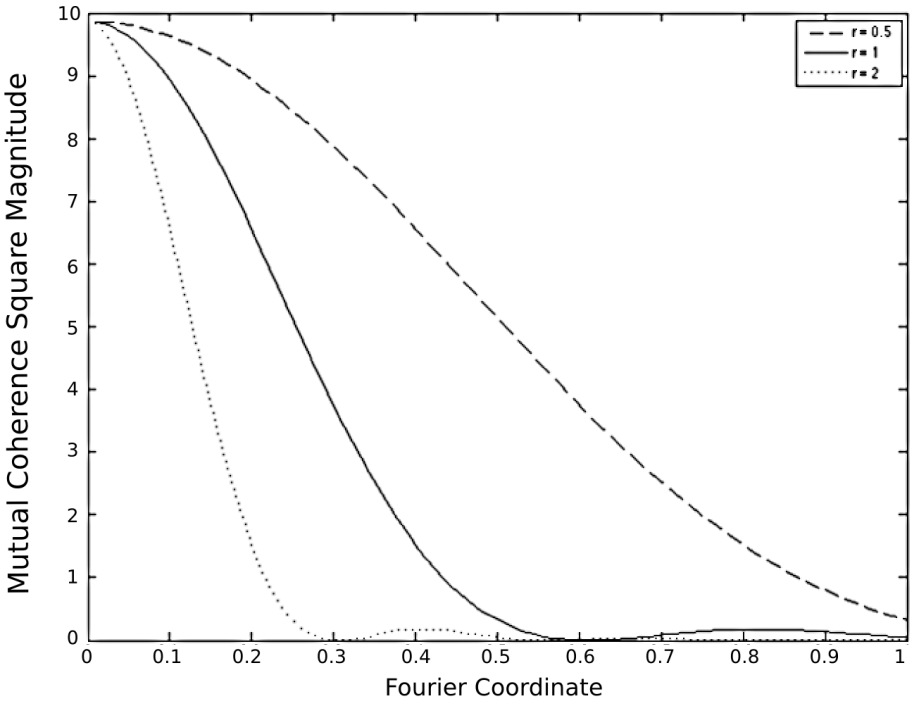


Fig. 9. Mutual coherence square magnitude of stellar disks of varying radii

## B. Example: Tracking Multiple Star Systems

Now, we wish to expand upon the first idea, the determination of binary angular separations. While two stars create a single interference pattern that can be easily measured, the cross-interference between stars in higher-order multiple star systems are not as simple. Although the systems are complex, each star is likely to be of similar brightness, so that the NLP problem is solvable with standard algorithms. For this reason, studying multiple star systems will provide a good example to develop the basic methodology for solving an image reconstruction problem as an NLP. Furthermore, a multiple star system has well-defined dynamics that we can use to demonstrate the application of dynamic estimation techniques as well.

### 1. Static Position Determination

First, we define the scene similarly to before, using a sequence of delta functions:

$$s(x,y) = \sum_{k=1}^{N} \alpha_k \delta(x - x_k, y - y_k). \tag{2.5}$$

Note that because we assume delta functions, these equations would not apply if any of the stars were resolvable by the system as a whole; the same work could be done with a more complete model, but it would add complexity without any additional insight. Determining the mutual coherence, according to equation (1.2), is straightforward:

$$\Gamma(u,v) = \sum_{k=1}^{N} \alpha_k \exp\left[-2\pi i(x_k u + y_k v)\right], \tag{2.6}$$

neglecting the constant scaling terms. Now, we similarly simplify equation(1.10) for the measurement, so that $M = \Gamma^*\Gamma$. Carrying out the cross-multiplications gives

$$M(u,v) = \sum_{k=1}^{N} \alpha_k^2 + \sum_{k=1}^{N-1} \sum_{l=k+1}^{N} 2\alpha_k \alpha_l \cos\left[2\pi((x_l - x_k)u + (y_l - y_k)v)\right]. \tag{2.7}$$

Assuming no variation over the detector apertures is valid in this case, since we have already defined that the system as a whole is incapable of resolving the target, and therefore each individual detector will be far below the threshold where this would contribute to the measurement.

In Figure 10, we plot the measurements as they vary over the Fourier plane for three randomly generated cases. Note that the scales are normalized by the minimum required radius of the system $r_{max}$ and the wavelength $\lambda$. Looking at these results, we are able to determine both the maximum Fourier coverage and a desirable sampling rate. The sampling rate is defined primarily by the largest cosine function, and thus the maximum expected separation, which we define as $r_{max}$. Based on this, and corroborated by the Figure, in order to sample this at the Nyquist limit, the system should sample the Fourier plane by at least $0.5\lambda/r_{max}$. The maximum diameter of the system will determine the minimum separation that one desires to measure ($\sim \lambda/r_{min}$). However, we may not need to measure the smallest separation, since each star interferes with all of the others, and the larger cosine patterns created by the more distant stars may provide enough information to determine their positions independently; a higher sampling rate will be valuable in distinguishing these components. Looking at these plots, a total coverage of 2-3$\lambda/r_{max}$ may be sufficient.

This allows us to design an array capable of measuring all of these variables simultaneously. For the case of four stars, we will be attempting to measure 12 state variables, giving us a minimum number of six detector assemblies (fifteen measurements), in order to have a well-posed problem. For the sake of reducing noise, an array of nine detectors and 36 measurements is appropriate, suggesting a Golay-9 array. A full-coverage radius of $2\lambda/r_{max}$ will give a sampling rate of $0.5\lambda/r_{max}$, exactly fulfilling our previously defined requirements. This array, and its Fourier coverage is

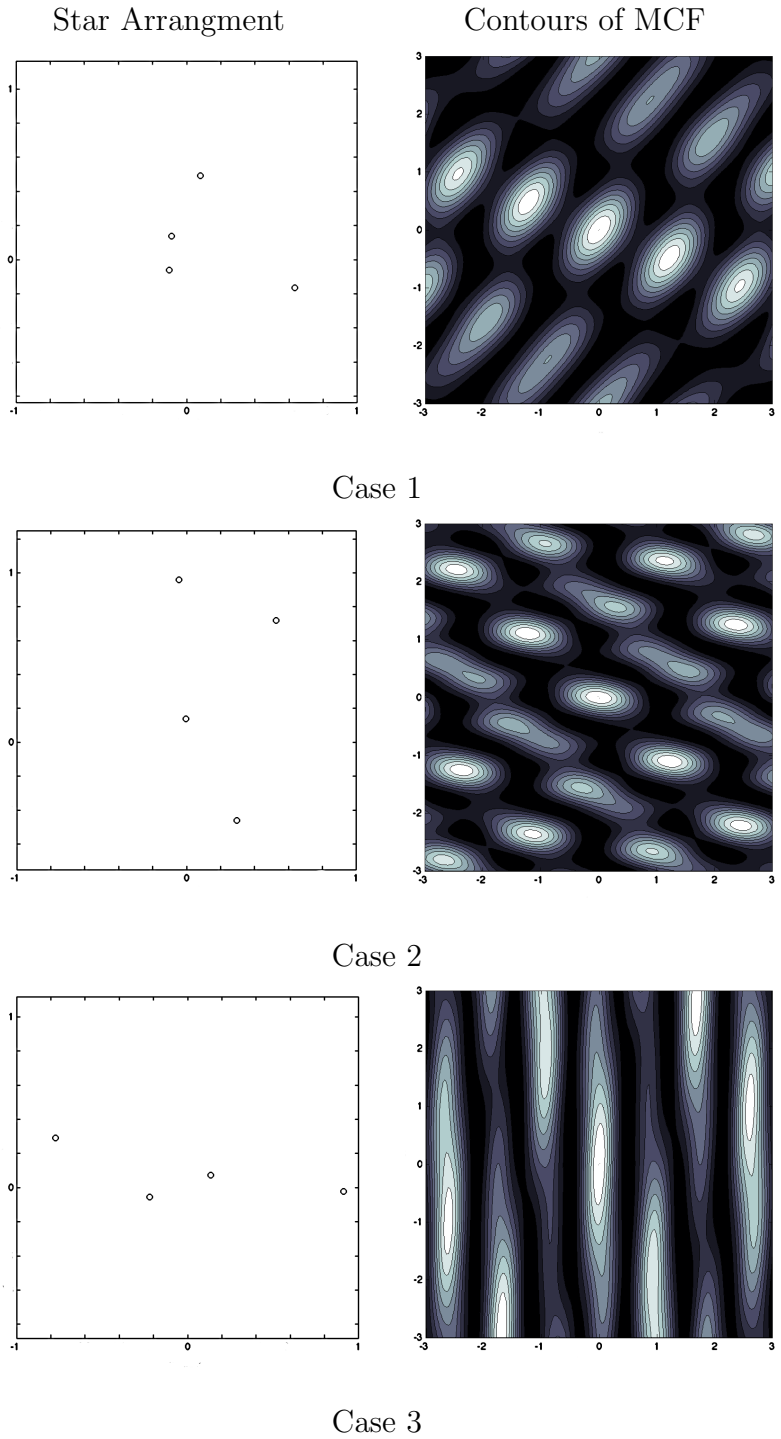


Fig. 10. Example star patterns and their coherence distributions

shown in Figure 11.

Now, in order to solve this problem with an over-defined set of noisy measurements, a least-squares solution method is a natural choice. In order to do this we define a cost function, and minimize the variance between the real measurements and those calculated from a set of estimated parameters, by varying those parameters. We define the cost function $J$ as

$$J = \sum_{n=1}^{N_m} W_n \left( \left( \hat{M}_n(\hat{\alpha}, \hat{x}, \hat{y}) + \delta \right)^{\zeta} - (M_n + \delta)^{\zeta} \right)^2, \tag{2.8}$$

and pose the problem as an NLP minimizing $J$ by varying $\hat{\alpha}$, $\hat{x}$, and $\hat{y}$, possibly subject to some known constraints. The emperical constants $\delta(<< 1)$ and $\zeta \sim O(1)$ are used to improve convergence.

After experimenting with solving this NLP, a few problems become apparent. The solution methods often seek solutions well outside the known maximum separations, finding the points that are multiples of the actual frequencies and coinciding with the sampling rate. For this reason, it is necessary to choose an NLP solver which accepts bounds on the potential solution. The *active-set search* algorithm employed by the *MATLAB* function *fmincon* was chosen to solve this problem, because it handles the problem well without relying on analytical derivatives [17]. However, this problem has many local minima; the algorithm finds the correct solution, indicated by a much smaller value of $J$, with a probability $\sim O(0.1)$. An inelegant but useful method for solving this problem is to simply iterate the solution multiple times with a different random initial estimates until a threshold for $J$ is passed. Because the solution time for this problem with only a few parameters is so much smaller than the time required for the observations, improving the convergence speed is not especially important. Each iteration takes $\sim O(30 \text{ sec})$, and an average of 10 iterations

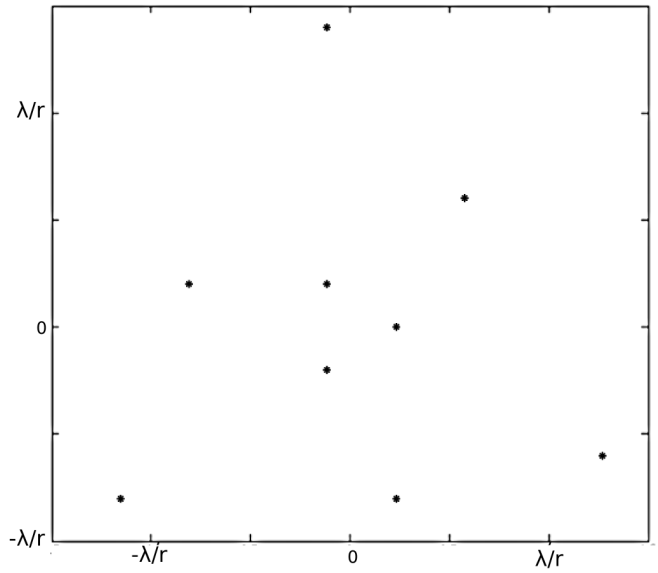


Array

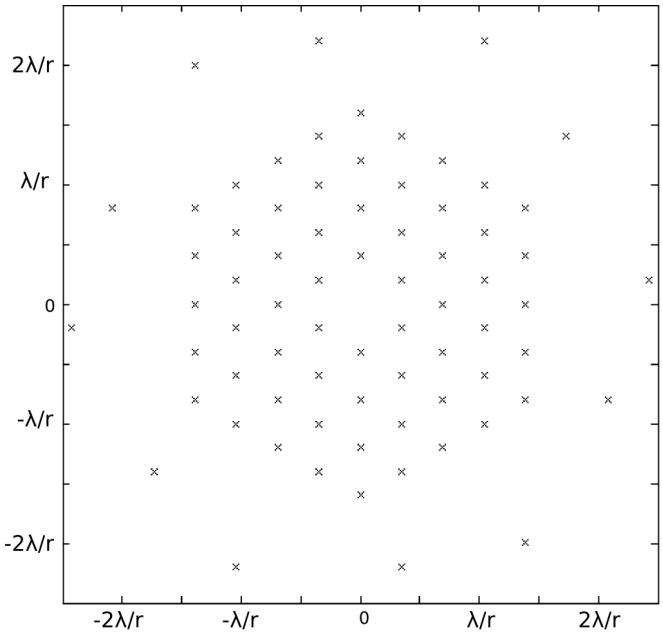


Fourier Coverage

Fig. 11. Array layout and Fourier coverage for multiple star tracking

Table I. Errors resulting from static multiple star position detections with varying SNR

| | SNR = 5 | | | SNR = 10 | | | SNR = 100 | | |
|---|---|---|---|---|---|---|---|---|---|
| Case | $\Delta\alpha^2$ | $\Delta\mathbf{x}^2$ | $J_f$ | $\Delta\alpha^2$ | $\Delta\mathbf{x}^2$ | $J_f$ | $\Delta\alpha^2$ | $\Delta\mathbf{x}^2$ | $J_f$ |
| 1 | 1.02 | 0.12 | 0.92 | 0.54 | 0.08 | 0.19 | 0.02 | 0.08 | 1.62e-3 |
| 2 | 0.34 | 1.25 | 2.09 | 0.52 | 1.66 | 1.24 | 0.34 | 1.97 | 1.09e-3 |
| 3 | 1.02 | 3.09 | 0.52 | 1.07 | 1.69 | 0.12 | 0.83 | 3.49 | 1.69e-2 |
| 4 | 0.19 | 0.02 | 0.68 | 0.85 | 0.53 | 0.13 | 0.20 | 0.27 | 9.52e-2 |
| 5 | 0.12 | 1.54 | 6.81 | 0.05 | 3.45 | 0.13 | 0.32 | 2.84 | 0.25 |
| 6 | 0.31 | 0.16 | 2.51 | 0.23 | 0.91 | 0.46 | 0.41 | 1.06 | 4.83e-3 |
| Mean | 0.50 | 1.03 | 2.26 | 0.54 | 1.38 | 0.38 | 0.35 | 1.62 | 0.06 |

are required to find the true solution, run with uncompiled *MATLAB* code on a 1.6 GHz Intel Core 2 Duo, with 2 GB of RAM. Note that the solution will have rotational and translational ambiguities, since only the position differences appear in equation (2.7), and the cosine function is symmetric about zero.

In order to understand the effects of noise, we take six random star arrangements, shown in Figure 12, and add random noise with a signal to noise ratio of 5, 10, and 100. The sum-square errors for both position and magnitude, as well as the final cost function, are shown in Table I. The position errors are measured away from their average value, to negate any issues associated with the translational ambiguities. Although there is a trend that higher SNR levels do improve the accuracy of the reconstruction, it is not a strong trend, probably due to the highly non-concave nature of the problem. This suggests that a requirement that SNR= 30 is sufficient for a good reconstruction.

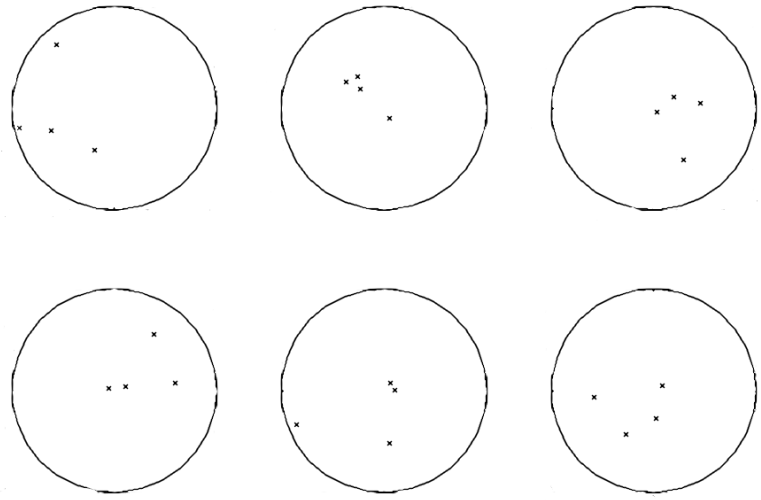

Fig. 12. Example cases for varying SNR study for multiple star positioning

In order to achieve this, we consider a four-star system observed from 50 parsecs away. Using the equation for SNR in (1.12), we assume the parameters

$$\begin{aligned} \alpha &= 0.9 \\ S &= 1 \text{ m}^2 \\ T_d &= 10^{-6} \text{ sec.} \end{aligned}$$

According to Planck's law, the number of photons at a given wavelength $\lambda$ for a blackbody emitter of temperature $T$ per unit area per solid radian per Hertz per second is

$$n = \frac{2}{\lambda^2} \frac{1}{e^{\frac{hc}{kT\lambda}} - 1} \tag{2.9}$$

which at 550 nanometers and with a stellar surface temperature of $5 \times 10^6$ Kelvin,

gives $n = 1.25 \times 10^{15}$ phot./m$^2$/radian$^2$/s/Hz. With four sun-sized stars at 50 parsecs, the total subtended area is $2.58 \times 10^{-17}$ square radians, so that $cT_c \langle I \rangle \approx 3.2 \times 10^{-3}$phot./m$^2$/s/Hz. Based on this, and given average values of $|\gamma|^2 = 0.5$, the required integration time to achieve the desired SNR of 30 is around 10 minutes. Dimmer objects will be more difficult to observe, but for astronomical targets these are very reasonable integration times.

## 2. Dynamic Modeling and Estimation

Now, if one requires significantly longer observation times, the stars will exhibit relative motion. If this is not accounted for, the results will be confused and inaccurate; however, since the motion of the stars relative to each other follow well known universal equations of motion we can instead use that motion to our advantage. Using estimation techniques for dynamic systems, that continued motion and knowledge of its properties can be used to determine the initial position, and thus all subsequent positions, with much more precision than the original static case. We also will be able to estimate the velocities and masses[1] of the stars explicitly. In terms of our NLP, we are estimating twice as many parameters, but taking many more measurements over time.

Given Newton's law of universal gravitation [18], the differential equation of motion for every star in the system of $N$ stars is

$$\ddot{\mathbf{x}}_k = \sum_{l=1}^{N, l \neq k} G \frac{m_l}{|\mathbf{x}_l - \mathbf{x}_k|^3} (\mathbf{x}_l - \mathbf{x}_k) \,. \tag{2.10}$$

Given the masses, initial positions and velocities, the system can be propagated forward, and from these propagated position values, we can estimate the expected mea-

[1] dependent on the precision of the known distance to the system

surements. Thus, we can define the measurement at any point in time as a function of the initial conditions and the time of the measurement. That is

$$M(u, v, t) = f(\mathbf{x}_0, \mathbf{v}_0, \alpha, m, t), \tag{2.11}$$

so that we can minimize the same cost function, summed over all baselines and measurement times, by varying the initial position and velocity, the brightness and the mass, creating another NLP.

For a test we use a quadruple star system arranged as a set of two mutually orbiting close binary pairs. Because these orbits must be numerically integrated, the selection of an initial estimate requires additional care. If a poor selection is made, the integration can lead to numerical errors and a disruption of the NLP solution process. For this reason, in our numerical simulations, we use the same algorithm to generate an initial estimate that we use to generate the truth arrangement. Defining this as dynamic estimation process, there are a number of options available, and it is not the purpose of this work to explore all of those options. Those options are more fully explored in texts such as *Optimal Estimation of Dynamic Systems* by Junkins and Crassidis [19]. Because of the need to impose boundaries, the same active-set algorithm used previously was sufficient to solve the problem.

The number of time-steps over which we measure the orbit is an important parameter not just for noise resilience, but also for convergence in the noiseless case. 100 time samples over a non-dimensional time period of 0.1 proved sufficient for convergence in our test cases, while 20 time samples was insufficient. Local minima are also still a problem for this algorithm, which we handle using the previous methodology for the static case. Solving for 5 random configurations as both dynamic and static problems, we show the relative errors as well as their ratios in Table II. Clearly

Table II. Comparison of static and dynamic estimation errors with SNR = 30

| **RMS Position Error** | | |
|---|---|---|
| **Dynamic** | **Static** | **Ratio** |
| $3.881 \times 10^{-3}$ | 1.2384 | 319.1 |
| $5.693 \times 10^{-3}$ | 1.4383 | 252.6 |
| $50.6056 \times 10^{-3}$ | 0.4968 | 9.8 |
| $1.8161 \times 10^{-3}$ | 1.7479 | 962.4 |
| $4.5805 \times 10^{-3}$ | 1.2818 | 279.8 |

the dynamic measurements greatly improve the resilience to noise, reducing the root mean square error by an order of magnitude or more in all cases, and by two orders of magnitude for most cases, while gathering more information about the system in the process. Note that this procedure does not allow for unknown perturbation forces in the model, nor does it account for three-dimensional aspects of the system such as out-of-plane viewing angles and off-ecliptic orbits. These could be included in the model as well; however, for this work it added unnecessary complications without yielding any more insight for the problem.

## C. Other Potential Scenarios

The previous example, with objects of similar magnitudes and well defined components is a relatively straightforward problem. Because the parameter variations cause the coherence fluctuations to be of similar magnitude with the signal itself, noise is not as significant an issue; because the parameters cause variations of similar magnitude to each other, the NLP can be solved relatively easily. Some other observations have

been considered that are more difficult, though not impossible. Measuring star spot positions on a distant star may be possible, but is at the edge of what is reasonably detectable. Measuring planetary motion has an even stronger imbalance in brightness, although use of the partial coherence effect may allow high-SNR observations.

### 1. Star Spot Measurements

Consider the problem of tracking star spots on a distant star. We define the scene as a disk of constant magnitude and a series of Dirac delta functions of varying magnitude representing the star spots:

$$s(x,y) = \alpha_0 \text{circ}\left(\frac{\sqrt{x^2+y^2}}{r}\right) + \sum_{k=1}^{N} \alpha_k \delta\left(x - x_k, y - y_k\right) \tag{2.12}$$

The Dirac delta approximation is appropriate because the system should not be able to resolve an individual spot. Now, the mutual coherence function $\Gamma$ is

$$\Gamma(u,v) = \alpha_0 r \frac{J_1\left(2\pi r\sqrt{u^2+v^2}\right)}{\sqrt{u^2+v^2}} + \sum_{k=1}^{N} \alpha_k \exp\left[-2\pi i\left(x_k u + y_k v\right)\right], \tag{2.13}$$

and the measurement $M$ is

$$\begin{aligned} M(u,v) \;=\; & \alpha_0^2 r^2 \frac{J_1^2\left(2\pi r\sqrt{u^2+v^2}\right)}{u^2+v^2} \\ & + 2\alpha_0 r \frac{J_1\left(2\pi r\sqrt{u^2+v^2}\right)}{\sqrt{u^2+v^2}} \sum_{k=1}^{N} \alpha_k \cos\left(2\pi(x_k u + y_k v)\right) \\ & + \sum_{k=1}^{N} \alpha_k^2 + \sum_{k=1}^{N-1} \sum_{l=k+1}^{N} 2\alpha_k \alpha_l \cos\left(2\pi((x_l - x_k)u + (y_l - y_k)v)\right), \end{aligned} \tag{2.14}$$

where the variables required to estimate the scene are the stellar parameters $\alpha_0$ and $r$, and the star spot parameters $\alpha_k$, $x_k$, and $y_k$, for each spot, giving $3N_s + 2$ unknowns, where $N_s$ is the number of estimated spots. Note that the values $\alpha_k$ will be negative, since a star spot has the effect of dimming the brightness at its location.

Now, there are four components to the equation (2.14), and it is instructive to understand what each component represents, and how it is best measured. The first component is the primary representation of the stellar parameters, and is equivalent to the measurement model for stellar diameters. As demonstrated above, measurements in the Fourier plane out to approximately $0.5r^{-1}$ are required to capture this component. Note that the third term indicates a dimming due to the starspots. This is not scientifically accurate, since spots actually cause an increase in brightness on the surface around the spot. However, our model does not capture this, because it would lead to more complexity with minimal benefit for this kind of initial study; any implementation would need to handle these variations in a more substantive manner.

The second and fourth terms of equation (2.14) are the more interesting terms, since they contain information about the positions of the spots. The second term, the cross term between the stellar disk and the spot locations, creates a modulating pattern directly related to the actual position of each spot independent of the others. This will allow the positions to be determined (with respect to the star center) without translational ambiguities. The fourth term, the cross-term between the spots contains information about their relative position.

Now, in order to understand the relative magnitude of the components, we want to plot sample values of equation (2.14) over a range away from the origin. We normalize the scene so that the the $\alpha_0 = r = 1$, so that the total brightness is $\pi$. At most, the relative brightness of a sunspot is around 0.1% of the total brightness [20], so we set a maximum value for $\alpha_k$ as $0.001 \cdot \pi \approx 0.03$. Using these values, and four star spots, we first consider the mutual coherence near the central spike from the main disk. Shown in Figure 13, the stellar disk is clearly dominant within a region less than $r^{-1}$.

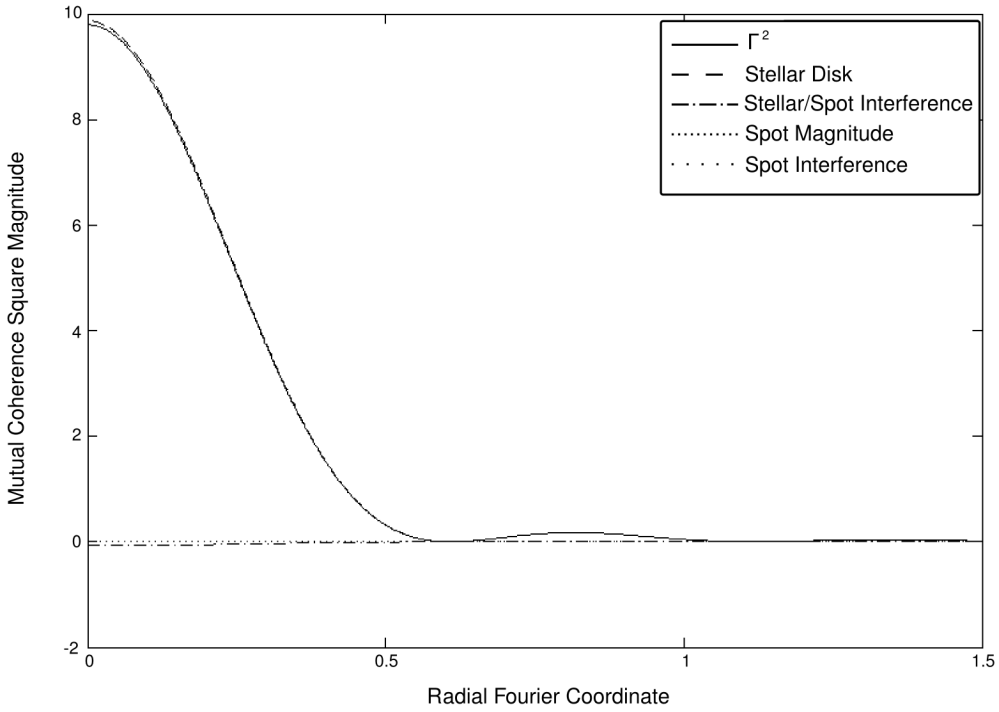


Fig. 13. Coherence magnitude of a star model near the central spike

Further away from the origin, as shown in Figure 14, the effects of the sunspots are more obvious. The third component is a strong DC component that the other components fluctuate about. The strongest components are the cross-terms between the spots, although the cross-terms between the stellar disk are still significant within this region as well. This is important because the second term is critical for eliminating translational ambiguities in the system. However, recall that we specified that the system is incapable of resolving an individual star spot, which we estimate as having a maximum diameter of $0.05r$, so it is unlikely that anything beyond $20r^{-1}$ would be of any value. Also note that the total coherence value is $\sim O(10^{-2})$, meaning that the signal to noise properties will be less favorable than near the central spkie.

This information informs how we design the system. First, the detector baselines must measure between $5r^{-1}$ and $10r^{-1}$ to get significant information from the star spots. Furthermore, in a more difficult task, this region must be sampled sufficiently to capture the wave patterns. Again, looking at the plot, the samples vary with a period of about $0.5r^{-1}$, suggesting that we need to sample the region at $0.25r^{-1}$. Based on this, we estimate that we require between 30 and 40 measurements along a single direction, and thus approximately 1000 measurements and 40 to 50 detector assemblies.

Observing Figure 13, the near-origin measurements in the Fourier field will be most useful in determining the stellar diameter and magnitude information, and for this information, SNR $\sim O(10)$ will be sufficient given the smoothness of the curve and the minimal impact of other effects. However, if one desires to obtain, useful information about the starspots in this region, the relative magnitude of the other components ($\sim$ 1%) means that an SNR $\sim O(10^3)$ would be required. Looking further out, again at Figure 14, in order to gain sufficient measurement of the starspot

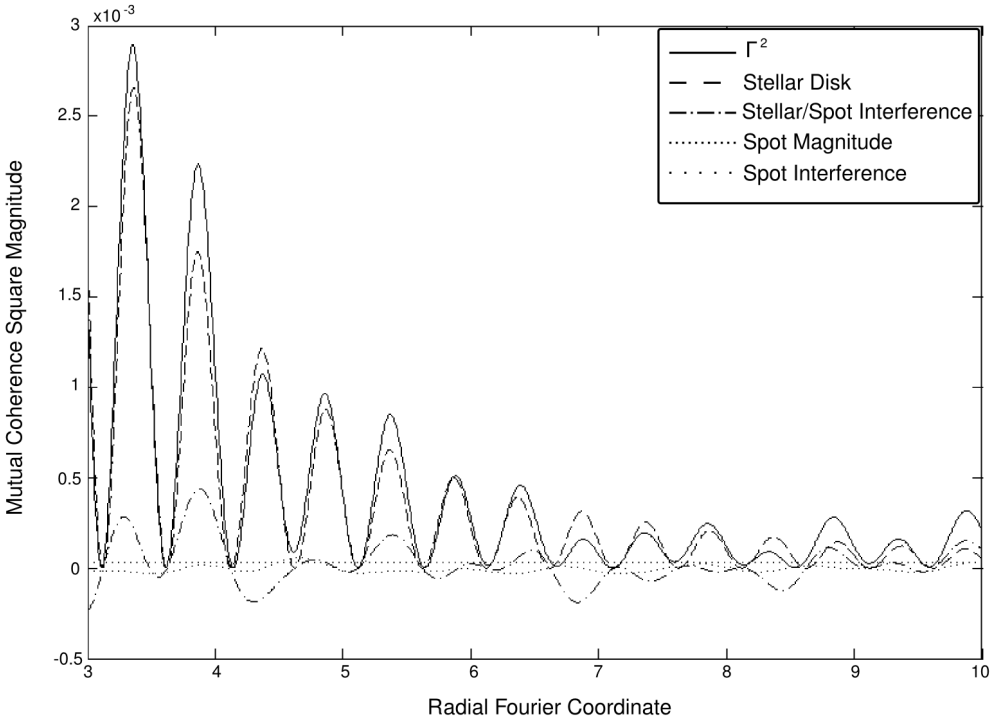


Fig. 14. Coherence magnitude of a star model far from the origin

components, an SNR closer to $\sim O(10^2)$ will be required for regions $\sqrt{u^2+v^2} \leq 5$ and a level $\sim O(10)$ beyond this point.

Again, using the equation for SNR in (1.12), observing a sun-sized star only 15 light-years away, with the more favorable parameters

$$\begin{aligned} \alpha &= 0.9 \\ S &= 4\text{m}^2 \\ T_d &= 10^{-8} \text{ sec} \end{aligned}$$

we again determine the required integration times. A sun-sized star at 15 light-years, has a total subtended area of $7.56 \times 10^{-17}$ radians$^2$, so that $cT_c \langle I \rangle \approx 10^{-1}$phot./m$^2$ /s/Hz. Based on this, and given approximate values of $|\gamma|^2$, the required integration times to achieve the desired SNR in each region are given in Table III.

Table III. Integration times required for desired SNR in star-spot tracking

| U-V range ($r^{-1}$) | $\lvert\gamma\rvert^2$ | SNR | $T_a$ (s) |
|---|---|---|---|
| 0-2 | $10^{-1}$ | 1000 | 7.7 |
| 2-5 | $10^{-4}$ | 100 | $7.7 \times 10^4$ |
| 5-20 | $10^{-5}$ | 10 | $7.7 \times 10^4$ |

These results, even with optimistic numbers, show that even with a very large array and subsequent large investment, the results are on the edge of observability. Because of the very small magnitudes of the star spots compared with the total star brightness, and the noisiness of intensity interferometry methods, this is a very difficult problem. The fact that the most useful measurements must be taken in the

far regions of the Fourier plane only make this worse, because they are more difficult for the NLP solvers to work with. This example, while demonstrating the possible capabilities of ICI, also shows the very significant shortcomings, particularly when dealing with low MCF values.

### 2. Tracking Extra-solar Planets

The discovery and study of extra-solar planets has been one of the most exciting areas of research in the past ten years. Mathematically, the results are the same as those for tracking multiple star systems; however, the differences in brightness is much more significant, with large gas giants being on the order $\sim O(10^{-7})$ the brightness of their star, and earth-like planets being closer to $\sim O(10^{-10})$ of the brightness of the star [21]. This difference in brightness, already problematic for the previous example of tracking star spots, is even worse in this case.

In traditional imaging optics, these situations are handled by coronagraphs that physically block the light from the parent star, allowing the dimmer objects (potentially including the corona) to be imaged. In our case, because the planets are much smaller spatially than their parent star, it may be possible to use the partial coherence effect to perform the same duty as the coronagraph. By sizing a system so that it is able to resolve the star, but not the planets, this problem can be reduced [12]. Obviously, a detector capable of resolving a star must be very large: a direct solution to this is to follow the STACEE project [22], and make use of large, reflective solar energy plants with massive apertures to do this.

# CHAPTER III

## EARTH IMAGING APPLICATIONS

There are many straightforward applications of ICI to astronomy. The application to earth-imaging, though very compelling, faces some unique challenges. To see the appeal of an ICI-based earth observation system, take the IKONOS commercial remote sensing satellite, shown in Figure 15, as a typical instrument for observations from low-earth orbit (LEO), for contrast. The 0.7-meter primary mirror in a 680-kilometer orbit is able to provide 1-meter resolution panchromatic images, at the theoretical diffraction limit of the instrument. [23] If one desired to achieve the same resolution imagery from a geostationary orbit (GEO), with the subsequent advantages in access and availability, a 37-meter telescope would be required. This is beyond the size of even the largest Earth-based telescopes, the Keck and Gran Telescopio Canarias, which measure only 10 meters in diameter. Clearly, to achieve even moderate resolution from a convenient orbit such as GEO, sparse deployable systems are necessary, making ICI a compelling option due to its low mechanical precision requirements.

However, there are a number of new limitations and considerations when applying an interferometric method with limited baselines to a system with a wide field of view, problems that do not apply to the astronomical case. Recall the previous discussion regarding the partial-coherence effect, where if any individual sub-detector has a diameter sufficient to resolve the source, the signal quality drops quickly to zero. When looking at an extended scene, such as the Earth, care must be taken to limit the field-of-view of each detector so that a usable signal is measured. In order to achieve this, without relying on microscopic optics and detectors, the individual optics must be imaging quality, with the sensor on the focal plane approximately equal in size

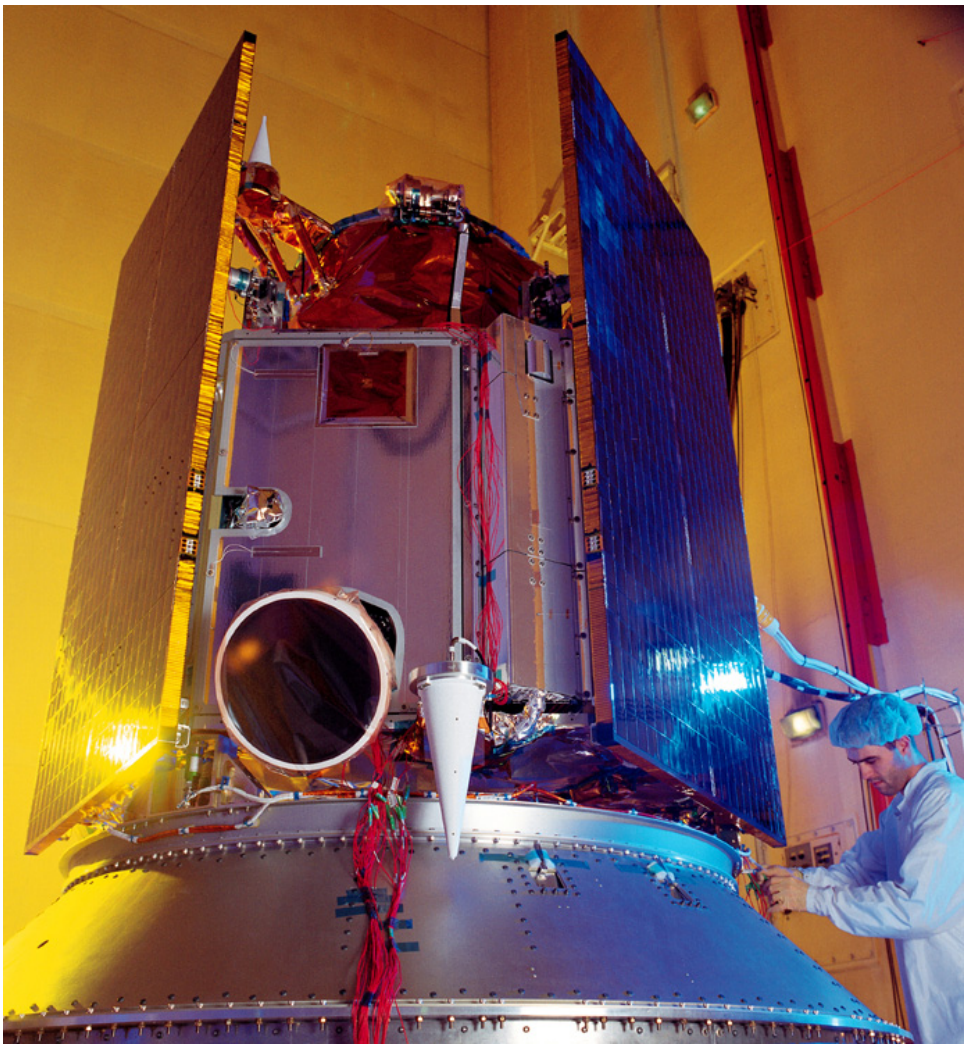

Fig. 15. IKONOS commercial remote sensing satellite

to the Airy disk for that system. For a series of moderate sized apertures, which we will soon see are necessary, this is not itself an especially arduous requirement, since the costs of optics scale exponentially with size, and moderate ($\sim$ 1 meter) mirrors will be of reasonable cost for a system of this magnitude. This also requires precise pointing of the optical assemblies, suggesting actively steerable secondary mirrors or focal plane arrays.

A second limitation is that the image must be measured within a short period of time in order to minimize the problems caused by motion on the target. This implies that the signal quality cannot be boosted beyond a certain point by increasing the integration time. It also implies that the techniques used to increase the Fourier plane coverage by rotating a linear array are unlikely to be usable, since a it would require very high rotational speeds; rather, an Earth-imaging ICI system would require full Fourier coverage in a static array. Note that these concerns are not directly affected by the following work.

The third significant variation is the way in which the phase retrieval problem changes from the astronomical case. While it is still possible to use finite bounds on the image, since the field of view of the detector is artificially limited, the ambiguity problems are much more significant. While the orientation of a stellar or planetary image would likely be of little consequence, the orientation of an image of the Earth's surface is critical to its interpretation. While there may be methods for using context clues to automatically reorient an image, this still poses a significant challenge. Any fully deployed system will require a robust, consistent, automated algorithm for reconstructing the image without ambiguities.

The final major impediments to developing an ICI-based earth-imaging system is the requirement for a very large swath width, or field-of-view. Context is critical to

the value of an image of the Earth's surface; increasing the swath width drastically increases the value of the system. Considering ICI as a system where a single pixel in each sub-aperture is *super-resolved* by cross-correlation measurements, it can be seen that a larger pixel with a much higher super-resolution factor is required in order to achieve this goal. Again, using IKONOS, which has a swath width of 11 kilometers, as an example, the maximum capability of the system is $11000 \times 11000$ pixels. An ICI image with a similar number of pixels, designed similarly to those previously for astronomy, would require nearly 22,000 sub-detector assemblies. While a reduction to only a $1000 \times 1000$ pixel image would improve this, it still requires a very large number of baselines in order to achieve images with sufficient context for an Earth imaging application. Following previous design methods, an earth-imaging system will always require a large number of very small apertures.

This solution poses two problems: one of practicality and complexity, and another of poor signal quality. The solution of building more, smaller optical packages for the detectors is viable only to a certain limit. As more telescopes are added, they will each have to be mounted and fitted with precise pointing controls. While smaller optics will be less expensive, the cost of the mounting and pointing systems will not necessarily decrease similarly. Thus, there will exist an optimal sub-aperture diameter that minimizes the cost, and it will be independent of the swath width requirements. That diameter may vary by orders of magnitude from that required for the desired swath width.

The second problem is even more limiting: as the super-resolution factor increases, the SNR drops drastically. The average value of the mutual coherence of a field falls logarithmically as the Fourier space is more finely sampled, in order to achieve higher super-resolution factors. Recalling equation (1.12), the noise mag-

nitude is largely independent of the MCF magnitude, meaning that the low MCF measurements associated with large super-resolution factors would be completely obscured by the read noise and photon noise of the system without extremely long integration times.

The balance between the need for a larger field-of-view and the associated problems, depending on the environment, will leave a very limited or even non-existent design space. However, the previous description of ICI as a super-resolution of a single pixel suggests an alternative: using multiple detectors on the same focal plane as *super-pixels* that are each super-resolved by a more moderate amount can. This provide a large field-of-view without the associated low MCF values. This decouples the swath-width from the aperture size, allowing packaging constraints to be considered, effectively expanding the design space. Potential designs with this modification include a smaller number of moderate-sized apertures rather than the massive arrays of small telescopes common to previous proposals.

Recently, while working in x-ray microscopy image reconstruction, Fienup has developed a process to use *transverse phase diversity* (TPD) to eliminate ambiguities and improve convergence of the phase reconstruction process. X-ray microscopy is a process for imaging small samples by passing a well-known x-ray illumination beam through a sample and measuring the intensity of the diffraction pattern in the far field. This measurement at sufficient distance is the magnitude of the Fourier transform of the field at the exit surface of the sample, allowing an image of the sample to be rebuilt using phase-reconstruction methods. By measuring multiple diffraction patterns as the illumination beam is translated transverse to the plane of the sample, the ambiguities of the reconstruction are removed and the resilience to noise are improved [24]. This is analogous to the super-pixel concept. This work was instrumental

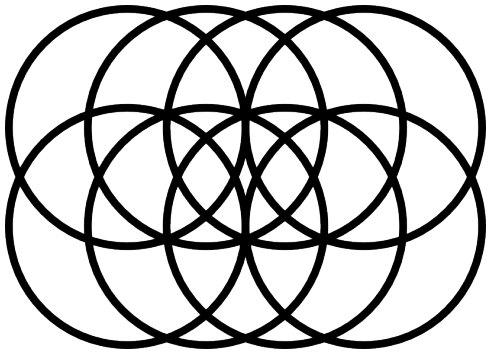

Fig. 16. Sample illumination beam pattern for transverse phase diversity

in the development of TPD-based ICI.

Treating the image reconstruction as a least-squares estimation process, where the measurements are the Fourier field magnitudes and the states are the reconstructed image pixel intensities, many standard non-linear programming approaches are valid; Fienup shows that the conjugate-gradient (CG) approach is particularly adept at handling these problems. The far-field intensity is measured multiple times, with the illumination beam translated across the sample for each consecutive measurement, with a pattern like that shown in Figure 16. The known overlap removes any uncertainty of the orientation of the image, and the phase diversity is automatically enforced by the least squares approach, with no need to explicitly define the phase relationship. Further development also allows imprecisions in the physical apparatus to be detected and accounted for by including the beam shape and centroids in the estimated state vector.

By treating the footprint of an individual super-pixel as the analog of the illumination beam with a particular translation, the application of TPD compliments and reinforces the previous concepts of using multiple super-pixels. The natural

diffraction of light and the sizing of the super-pixels allows the overlapping footprints necessary for sufficient phase diversity measurements. It is also possible that a transverse scanning pattern could be used in a similar way, although for an earth-imaging application, where "snapshot" images are desired and SNR is likely to be marginal, this is not an appealing solution. The two concepts together have the potential to mitigate the field-of-view problem, eliminate any concerns about ambiguities, and improve the consistency of phase reconstruction.

## A. Focal Plane Design

Previous ICI experiments and theoretical designs have relied on a single-pixel high-speed photodetector as the entire focal plane apparatus. Earth-looking systems particularly require that the active area of the sensor be smaller than the diffraction limited spot of the telescope, since the field-of-view must be intentionally limited in order to avoid issues related to partial coherence. The footprint of this detector on the ground will be the physical pixel shape convolved with the point spread function, as shown in Figure 17. This "spreading" of the pixel due to diffraction can be used to allow multiple distinct detectors on the same focal plane to achieve the same effect as the translating beam in Fienup's study.

A grid of detector surfaces, such as the example in Figure 18, will use the natural diffraction of light within a finite aperture to achieve the necessary transverse phase diversity measurements. The key design factors are that the detector separations are significantly less than the size of the diffraction limited spot, and that the detectors themselves are no larger than the diffraction limited spot. Beyond this, other important considerations are to achieve the desired swath width while maintaining enough overlap to gain an advantage from the phase diversity measurements

(a) Detector pixel shape

(b) Point spread function

(c) Detector footprint

Fig. 17. Footprint of a single detector in a diffraction limited system

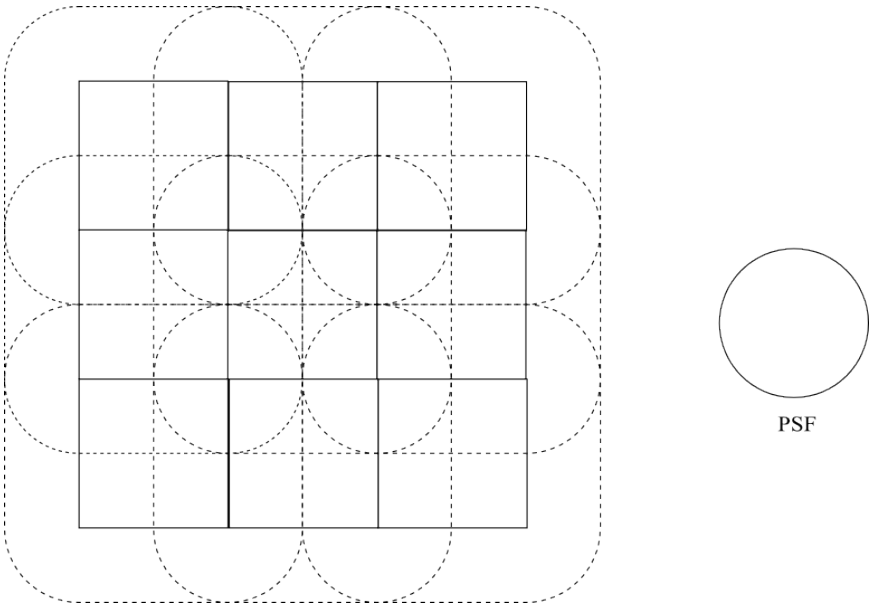


Fig. 18. Example of a $3 \times 3$ TPD detector grid layout

and ensure convergence.

In order to understand the super-pixel arrangement requirements, a study was conducted to determine the effects of varying the amount of finite support (i.e. known black space), the number of detectors on the focal plane $N_p$, the amount of overlap, and the total measurement to state ratio $R_m$. Multiple layouts and their reconstructed images are shown in are shown in Figure 19, and the results and various statistics for these cases, both with and without noise, are shown in Table IV. The reconstructed images (for the noiseless cases) are shown in Figure 20. Note that the overlap percentage refers to the percentage of the pixels that are covered by more than one super-pixel.

These results, while insufficient to determine any hard limits for convergence, do give some strong evidence of the requirements. Most importantly, we compare

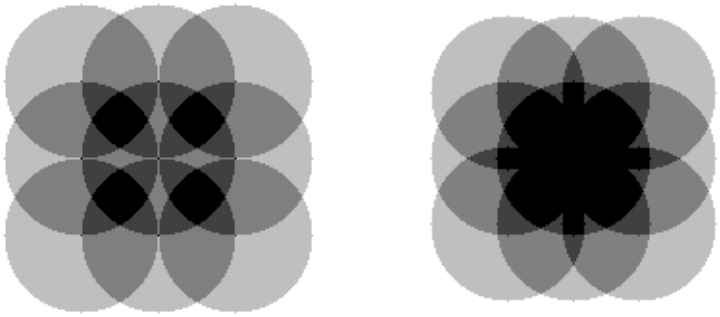

Case 1 Case 2

Case 3 Case 4

Case 5 Case 6

Fig. 19. Example of super-pixel arrangements for comparison of convergence properties

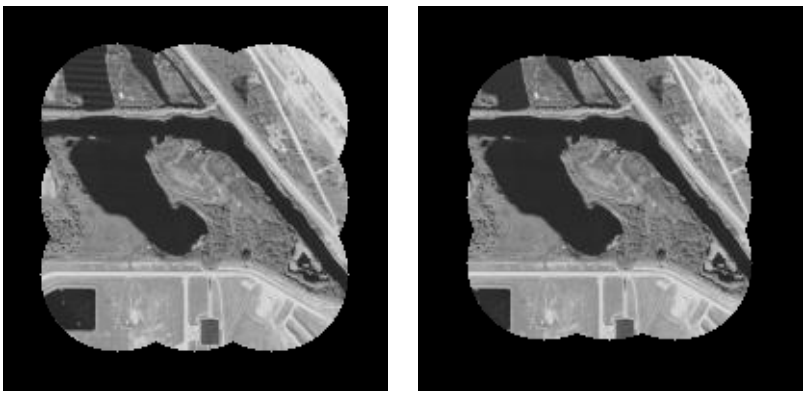

Case 1



Case 2

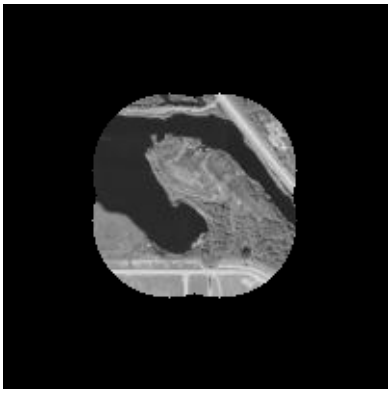

Case 3

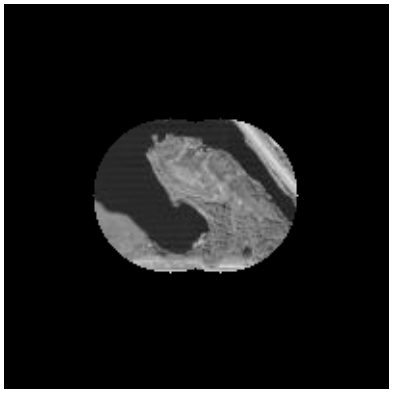

Case 4

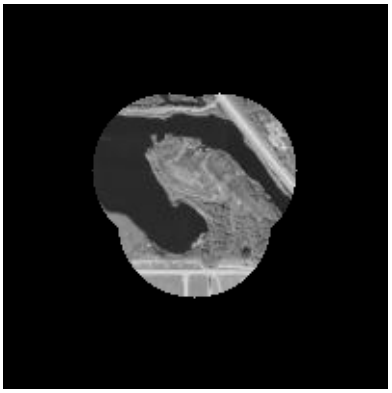

Case 5

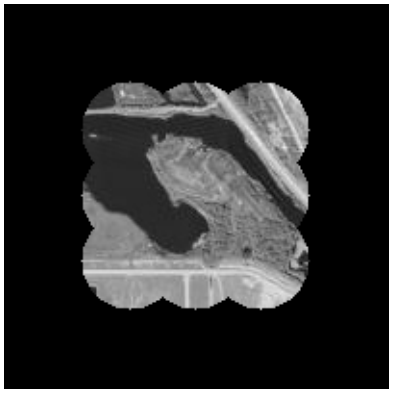

Case 6

Fig. 20. Reconstructed images for each of the super-pixel test cases, using the noise-free simulation

Table IV. Statistics of TPD reconstruction with various pixel layouts

| | | | | SNR = $\infty$ | | SNR = 10 | |
|---|---|---|---|---|---|---|---|
| Case | $N_p$ | % Overlap | $R_m$ | $J_f$ | $\sigma_{px}$ | $J_f$ | $\sigma_{px}$ |
| 1 | 23649 | 60.3 % | 15.2 | 0.105018 | 4.03e-3 | 47.57 | 1.02e-2 |
| 2 | 20169 | 66.4 % | 17.8 | 4.3e-16 | 1.73e-10 | 54.13 | 6.29e-3 |
| 3 | 9773 | 61.0 % | 16.37 | 6.20e-16 | 1.63e-12 | 39.73 | 4.86e-3 |
| 4 | 7061 | 42.3 % | 11.33 | 0.32362 | 4.03e-3 | 28.19 | 5.17e-3 |
| 5 | 8656 | 50.2 % | 13.8 | 3.42e-14 | 5.90e-10 | 37.68 | 4.96e-3 |
| 6 | 12809 | 36.5 % | 28.1 | 0.43458 | 7.92e-3 | 33.16 | 8.57e-3 |

the three systems that converge, cases 2, 3 and 5, with the remainder that do not. Convergence is indicated by the errors for the noiseless case being reduced to arbitrarily small values, as well as the lack of large-scale artifacts in the reconstructed images. The critical factor appears to be the area of the overlapping region. Particularly notice the differences between cases 1 and 2: both have nine super-pixels of the same size, yet by reducing the separation slightly, and increasing the amount of overlap, the system is moved into a region of convergence. However, this is not well represented by the simple percentage of overlap, given that case 1 has a high overlap percentage yet does not converge, while cases 3 and 5 are significantly lower. Rather, it seems that increasing the overlap so that the center-to-center distance is less than the diameter of the super-pixel is the most valuable design rule.

While the overlapping region is the overriding concern, there are some other considerations as well. Case 4 appears to have sufficient overlap; however, it only provides phase diversity in one direction, allowing sinusoidal artifacts to develop in

the perpendicular direction. Looking at case 5, however, the two directions need not be orthogonal; that is, as long as the super-pixels are not all co-linear, this will not be a problem. A more surprising result is that a higher measurement ratio $R_m$, does not have any straightforward effect on the noise resilience, indicated by the pixel variance values. This may be a result of the fact that all of the measurement ratios are very high, so the variations between them are insignificant. However, for our case, described in more detail below, the measurement ratio will be lower, so this may be a more significant factor.

## B. Phase Reconstruction Methods

Again, we take the phase reconstruction process as a least-squares estimation problem, using the MCF measurements to estimate the image pixel intensities. Because it is a very large, non-linear problem with poor initial estimates, a first-order approach such as a steepest-descent approach is needed, rather than the fast-converging second-order approaches used previously. Fienup has found that the conjugate gradient method is especially powerful for this problem.

While the concept is similar to reconstructing images in x-ray microscopy, the specifics of the phase reconstruction for ICI vary in important ways, generally ways that make the reconstruction problem more difficult. These primarily relate to the sampling of the Fourier space. Describing the scene, including finite constraints as an $N \times N$ pixel grid, while the size of an individual super-pixel is $M \times M$ pixels, where $M < N$ by at least an order of magnitude, then x-ray microscopy retrieves an $N \times N$ sampling of the Fourier field for each super-pixel, while ICI will only obtain an $M \times M$ sampling. This reduces the measurement ratio significantly. Furthermore, the x-ray detector is a CCD or CMOS sensor with a regular rectangular grid, allowing well

defined and computationally inexpensive fast Fourier transforms (FFT) to be used. For ICI, an irregular grid is more likely to be used.

Also, closely related to the sampling rate, the averaging of the coherence over the aperture surfaces is more significant with ICI. While the sensor grid in x-ray measurements does some averaging over the pixel surfaces as well, the areas are much smaller, so that treating them as discrete measurements is a very good approximation. However, since the sampling region of an ICI measurement is around the same size as the coherence region, the variations of the MCF within that region are more significant. This means that the estimation routines must explicitly consider the integrals over the aperture surfaces, making the routines more computationally expensive. Additionally, while it is beyond the scope of this work, the pointing and beam-shape errors will have significantly more degrees of freedom than in the Fienup's work, since it will have to account for errors in each individual optical system rather than a single illumination beam.

### 1. Conjugate Gradient Method and Analytical Gradients

Following Fienup's development, we define our problem as an NLP, minimizing the variance in the measurements by modifying the estimated image. In order to do this, we again define a cost function

$$J = \sum_{k=1}^{N_p} \sum_{l=1}^{N_d} \sum_{m=l+1}^{N_d} W_{k,l,m} \left( \left( \hat{M}_{k,l,m} + \delta \right)^{\zeta} - \left( M_{k,l,m} + \delta \right)^{\zeta} \right)^2, \tag{3.1}$$

where $k$ is the index for the detector pixel, $l$ and $m$ define the baseline pair, $M_{k,l,m}$ is the actual measurement, $\hat{M}_{k,l,m}$ is the estimated measurement. $W$ serves as a weighting matrix.

Using equation (1.10), eliminating the constant terms and employing the van

Cittert-Zernike theorem, the measurement from a detector pair baseline is defined as

$$M_{k,l,m} = \iint_{u,v} \mu(u - u_{lm}, v - v_{lm}) \left|\mathrm{FT}\left[s(x,y) \cdot p(x - x_k, y - y_k)\right](u,v)\right|^2 du\, dv. \quad (3.2)$$

The variables $(u, v)$ are the coordinates in the Fourier plane, $\mu$ is the averaging mask that causes the partial coherence effect, and is defined as the convolution of the aperture functions of the detectors, and $p$ is the detector footprint projected onto the surface. The function $s$ is the scene under observation. The estimated measurement $\hat{M}$ is calculated using the same formula, using the estimated scene $\hat{s}$.

The conjugate gradient search for the minimum of $J$ is initialized as a steepest descent, determining the gradient and performing a line search in the opposite direction for the minimum point. The process is then iterated in a similar manner, using the steps shown in Table V. The main modification to the steepest-descent search is the addition of the term $\beta$ which adapts to the non-orthogonal space and allows faster convergence. For all of the results in this paper, we used $\beta = \min[0,\ \beta^{PR}]$, which insures convergence by resetting the conjugate to steepest-descent if the term becomes negative [25]. For all cases, an initial guess of $s(x, y) = 0$ was sufficient for convergence.

In order to use the CG method, we must calculate the analytical derivatives of the cost function with respect to the estimated state, in this case the estimated image $\hat{s}$, in order to obtain the gradient. Calculating this:

$$\begin{aligned} \frac{\partial J}{\partial \hat{s}(x,y)} &= \sum_{k=1}^{N_p} \sum_{l=1}^{N_d} \sum_{m=l+1}^{N_d} 2W_{k,l,m} \left( \left( \hat{M}_{k,l,m} + \delta \right)^{\zeta} - \left( M_{k,l,m} + \delta \right)^{\zeta} \right) \\ &\quad \cdot \zeta \left( \hat{M}_{k,l,m} + \delta \right)^{\zeta - 1} \frac{\partial \hat{M}_{k,l,m}}{\partial \hat{s}(x,y)}, \end{aligned} \quad (3.3)$$

$$\frac{\partial \hat{M}_{k,l,m}}{\partial \hat{s}(x,y)} = 2p(x - x_k, y - y_k) \mathrm{FT}^{-1} \left( \mu(u - u_{lm}, v - v_{lm}) \hat{\Gamma}(u,v) \right). \quad (3.4)$$

Table V. Iterative steps of the conjugate gradient method

| | |
|---|---|
| Compute Steepest Descent | $\Delta\hat{s}_n = -\nabla_s J$ |
| Compute $\beta$ (select one of the options) | $\beta_n^{FR} = \dfrac{\Delta\hat{s}_n^T \Delta\hat{s}_n}{\Delta\hat{s}_{n-1}^T \Delta\hat{s}_{n-1}}$<br>$\beta_n^{PR} = \dfrac{\Delta\hat{s}_n^T (\Delta\hat{s}_n - \Delta\hat{s}_{n-1})}{\Delta\hat{s}_{n-1}^T \Delta\hat{s}_{n-1}}$<br>$\beta_n^{HS} = \dfrac{\Delta\hat{s}_n^T (\Delta\hat{s}_n - \Delta\hat{s}_{n-1})}{\Lambda\hat{s}_{n-1}^T (\Delta\hat{s}_n - \Delta\hat{s}_{n-1})}$ |
| Update conjugate direction | $\Lambda\hat{s}_n = \Delta\hat{s}_n + \beta_n \Lambda\hat{s}_{n-1}$ |
| Line search for new minimum | $\hat{s}_{n+1} = \min_{\alpha} J(\hat{s}_n + \alpha\Lambda\hat{s}_n)$ |

Due to the linearity of the Fourier transform, it is possible to improve the computational efficiency by summing the components corresponding to a particular pixel before taking the inverse transform:

$$\frac{\partial J}{\partial \hat{s}(x,y)} = \sum_{k=1}^{N_p} 4p(x-x_k, y-y_k)\mathrm{FT}^{-1}\left[\sum_{l=1}^{N_d}\sum_{m=l+1}^{N_d} W_{k,l,m}\left(\left(\hat{M}_{k,l,m}+\delta\right)^{\zeta}\right.\right. \tag{3.5}$$
$$\left.\left. -\left(M_{k,l,m}+\delta\right)^{\zeta}\right)\zeta\left(\hat{M}_{k,l,m}+\delta\right)^{\zeta-1}\mu(u-u_{lm}, v-v_{lm})\hat{\Gamma}(u,v)\right].$$

This development is equally valid as both a continuous and discrete Fourier transform, except for some scaling issues that can occur with different FFT implementations. Additional gradient calculations will be required to accommodate system state error estimation.

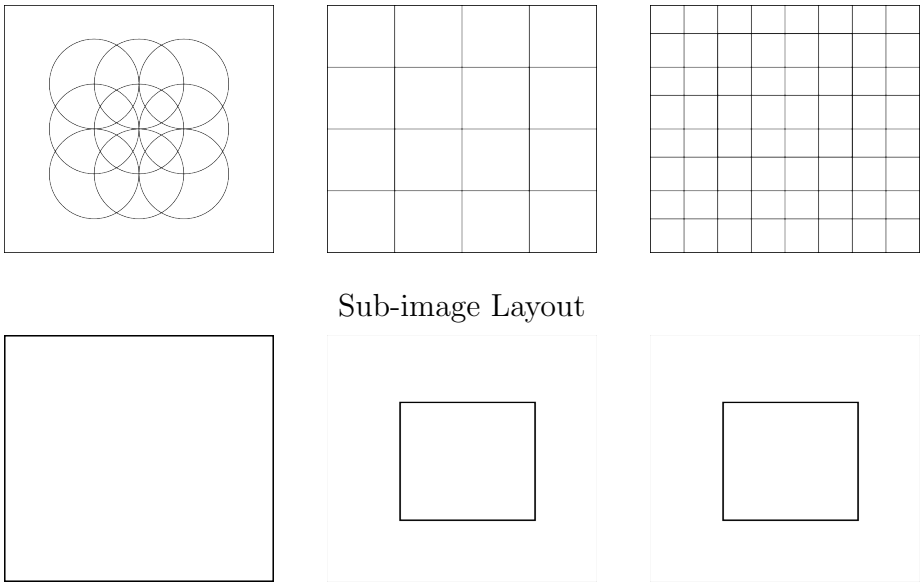


Fig. 21. Super-pixel layout and Fourier transform size for three examples used to test varying Fourier sampling rates

### 2. Results with Coarse Fourier Sampling

In order to understand the effects of the Fourier sampling rate, we compare a few cases. The first is a direct implementation of the conjugate gradient method with a full resolution Fourier measurements for nine overlapping circular fields-of-view, as done previously. The second splits the $200 \times 200$ image into nine overlapping $100 \times 100$ squares, with the $100 \times 100$ transform of each as the measurements. The final example again splits the same image into $100 \times 100$ sub-images, but over-samples the region significantly more, using 25 offset measurements. These layouts are shown in Figure 21.

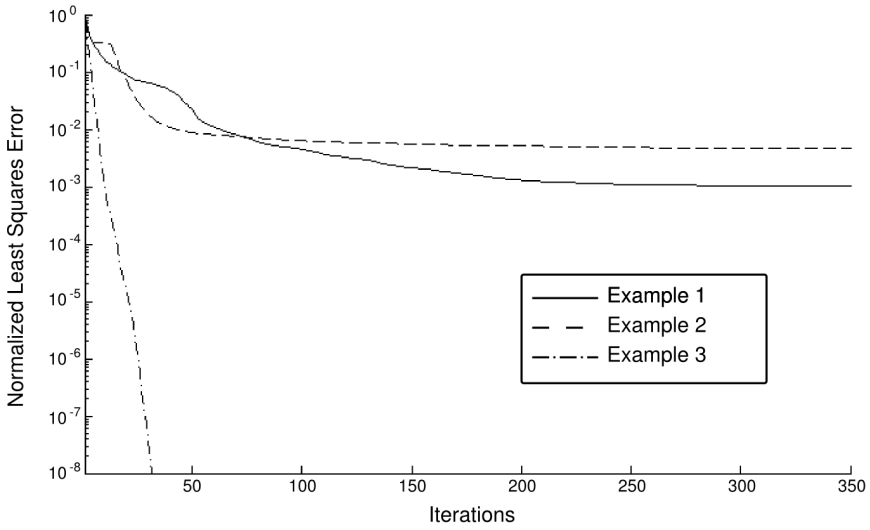


Fig. 22. Convergence of examples varying the Fourier sampling rate

When these three examples are run, the first case converges very quickly to duplicate the image within the field-of-view exactly when run without noise, as we'd expect from previous results, while the the third case converges to a recognizable solution that still leaves considerable, mostly periodic errors. The second solution however does not come to an even marginally acceptable solution, leaving only the rough outline of the basic shapes in the system. The convergence rate is shown in Figure 22, and the final reconstructed images are shown in Figure 23.

Based on this, the measurement of the full transform appears to provides significant advantages. We speculate that this might be due to uncertainties in the final Fourier transform of the estimated image, caused a 'blurring' over the full transform. Decreasing the spacing between the individual fields-of-view, as in case 3, improves the results. Unfortunately, it is difficult to determine the causes of convergence problems for a high-degree-of-freedom NLP problem, but a better understanding of this

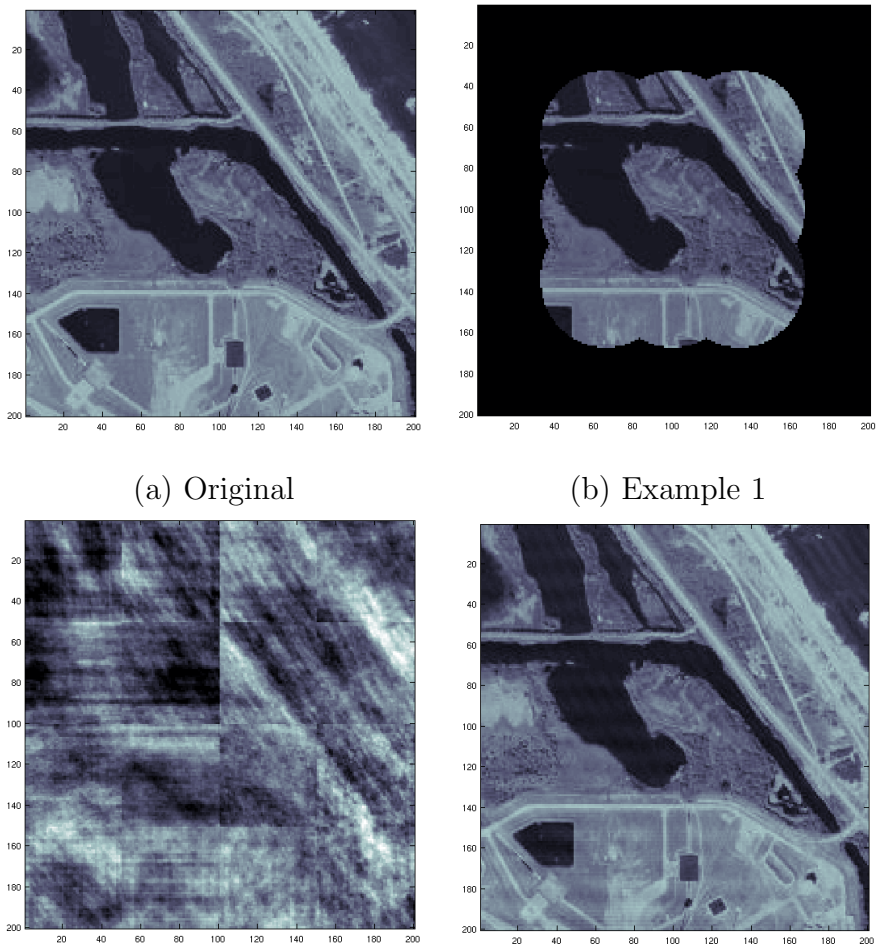

(a) Original (b) Example 1

(c) Example 2 (d) Example 3

Fig. 23. Reconstructed images for the three examples varying the Fourier sampling rate

problem, as well as potential solutions, would improve the phase retrieval problem significantly. This is important future work.

## C. Design Implications of Multi-Pixel Transverse Phase Diversity

By applying TPD and multiple super-pixels to the basic ICI concept, we are able to eliminate the strong coupling of the number of pixels in the final image to the number and size of sub-apertures, an extremely limiting factor when discussing earth-looking space-based imaging. Due to the partial coherence effect, and the finite sampling rate of the Fourier field, for a larger field-of-view, more and ever smaller detector assemblies are required, requiring $N_d > 2\sqrt{N_{px}}$ for a well posed problem, where $N_d$ is the number of detectors and $N_{px}$ is the number of final image pixels. When considering attempts at very high super-resolution factors, the mean square coherence values over the Fourier plane are very small ($\sim O(10^{-6})$) which leads to a drastic reduction in signal to noise, as would be expected from equations (1.11) and (1.12).

Consider a sample concept of a GEO imager attempting 5-meter resolution with a 1-kilometer square field of view at the 550-nanometer wavelength. The overall diameter of the device would be 5.5 meters, with 2.7 centimeter detector assemblies, so that their diffraction limited spots would be one kilometer in the linear dimension. A 2:1 measurement ratio, to ensure phase reconstruction convergence and accommodate noise, would require 400 detector assemblies; if a nearly full aperture (75%) is desired for SNR reasons, 31,000 detector assemblies would be required. While it is true that smaller apertures are going to be cheaper individually, with the additional requirements on pointing precision necessary for ICI with an extended scene, the overall costs of the optics, pointing systems and other components for this huge number of detectors would make it much less cost effective. However, using TPD-modified ICI, the

size of the detector assemblies can be selected with some independence from the FOV requirement, allowing fewer moderate sized apertures to fulfill the same requirement. This can allow a more cost effective, and generally more optimal design.

The recent JASON study has gone even further to show that the reliance on ever larger numbers of small telescopes to increase the field-of-view is not a viable design path [26]. Consider the simplified form of equation (1.12). The SNR is proportional to the square magnitude of the the mutual coherence, meaning that it is in our best interest to keep the MCF $\gamma$ as close to unity as possible. Taking a sample image of Cape Canaveral, shown in Figure 24, we measured the mean square mutual coherence of various-sized subsets of the image. The results of this are shown in Figure 25, and show that the value of $|\gamma|^2$ decrease logarithmically with the number of pixels, as does the SNR. Thus in order to maintain a relatively high MCF ($\sim O(10^{-2})$), the super-resolution factor should be kept on the order of $\sim O(10)$. This does limit the design space considerably, but the application of TPD and multiple super-pixels means that a useful ICI-based design with a reasonable field-of-view is not infeasible, as it would be without the application of these methods.

Applying TPD to the proposed requirements above, and taking the super resolution factor to be 10, the detector assemblies would need to be able to resolve a 50-meter feature, requiring a set of 0.5-meter apertures, which, while large, are not unreasonable for a project of this scale. Furthermore, only 40 apertures would be required to achieve a 2:1 measurement ratio, and only 91 would be required to achieve a 75% filled aperture. All of this is achieved by using 400 super-pixels arranged in a $20 \times 20$ grid on the focal plane. This would be significantly more cost effective than deploying a large aperture for a true telescope to achieve the same resolution.

Fig. 24. Sample image of Cape Canaveral used for considering coherence magnitude

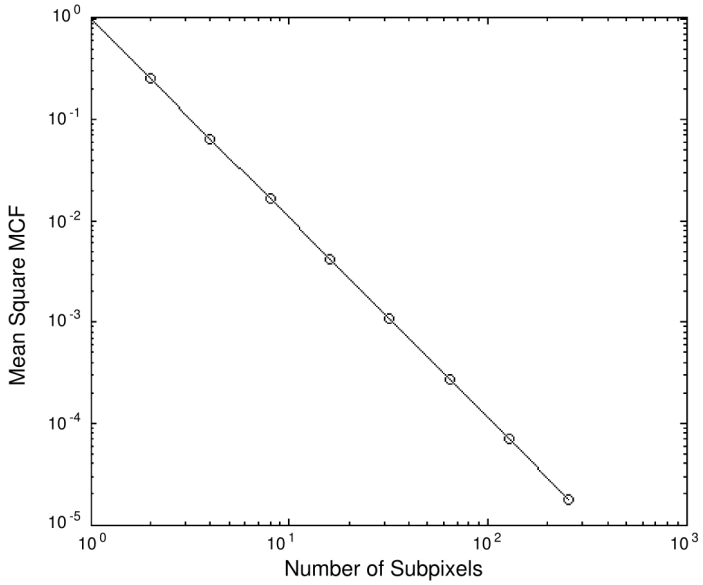


Fig. 25. Dependence of the mean square mutual coherence value on the number of pixels in an image

## D. Sample System Design and Phase-Retrieval Simulation

As a demonstration of the variations necessary for an TPD-based ICI system, we design and simulate a demonstration system capable of 5-meter ground sample distance (GSD) with a 320-meter swath width from GEO altitude at 550-nanometer wavelength. The relatively small swath-width is not indicative of a limit on the system, but was chosen solely to reduce computational time. The system is based around a Golay-9 sparse array, with 0.8-meter sub-aperture diameters. This diameter is an *a priori* selection in the simulation, and was selected because we expect that optics smaller than a meter will be relatively inexpensive, and because it gives acceptable results with a Golay-9 array at the desired resolution. The nominal diameter of the Golay array is calculated from the desired GSD $\delta x$, the altitude $h$, wavelength $\lambda$, and the equation of the diffraction limit

$$D_{nom} = 1.4\frac{\lambda \cdot h}{\delta x} \approx 5.6 \text{ meters.} \tag{3.6}$$

This gives the array arrangement shown in Figure 26. By design, the Golay-9 array gives full Fourier plane coverage (Figure 27) out to the specified diameter. Note that the spacing of the peaks indicates the sampling rate of the Fourier coverage.

The 0.8-meter sub-apertures with the 5.6-meter nominal diameter gives us a super-resolution factor $\alpha$ given by

$$\alpha = \frac{\theta_{sub}}{\theta_{full}} = \frac{1.4\lambda/D_{sub}}{1.4\lambda/D_{nom}} = \frac{D_{nom}}{D_{sub}} \approx 7. \tag{3.7}$$

Increasing the diameter of the sub-apertures will reduce the super-resolution factor, but will also require a larger number of super-pixels to achieve the same swath width. For this demonstration, a super-pixel size $\Delta x = 0.7\lambda/D$ was chosen, fitting the crite-

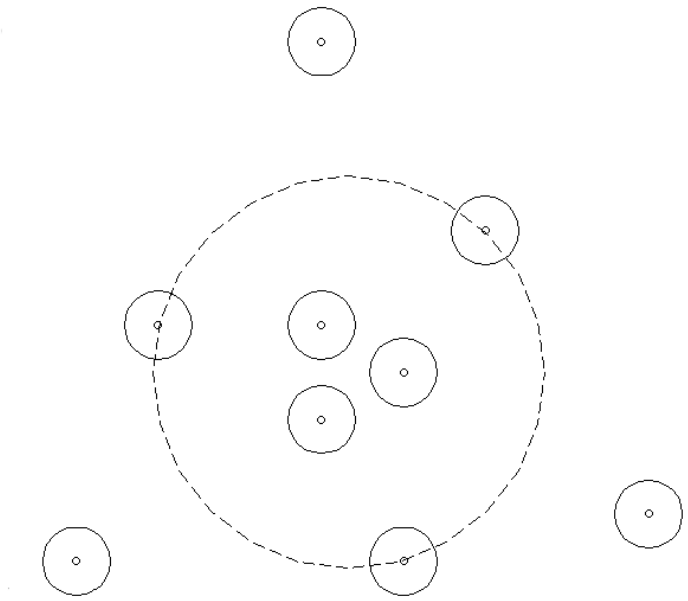

Fig. 26. Physical aperture layout of example TPD-ICI system, overlaid on nominal full aperture

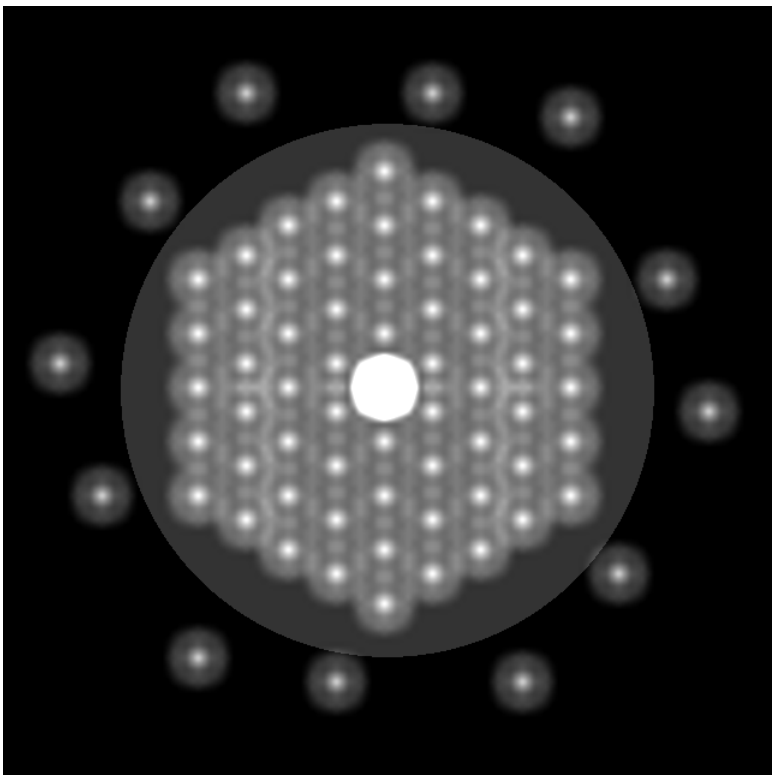

Fig. 27. Fourier plane coverage of example TPD-ICI system, overlaid on MTF of nominal full aperture

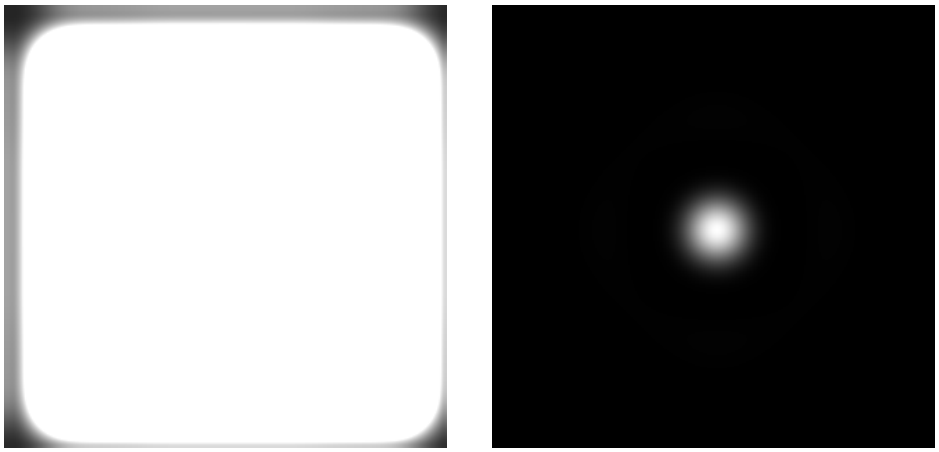

Total swath area of system  Footprint of individual super-pixel

Fig. 28. Field of view and super-pixel size of example TPD-ICI system

rion that

$$\Delta x < 1.4\frac{\lambda}{D_{sub}}, \tag{3.8}$$

In this case we chose a significantly smaller value, half of the diffraction limit for the sub-apertures, in order to improve the performance. A smaller super-pixel size gives a larger percentage of overlap, which improves convergence and reduces artifacts, as demonstrated in the previous sections. This must be traded against the larger number of super-pixels required, and the subsequent increased computational cost for correlation calculations and phase reconstruction. Given all of this, the super-pixel grid consists of 324 super-pixels in an $18 \times 18$ grid, giving a total of 11,664 correlation measurements. These are used to estimate 4,096 image pixels, giving a measurement ratio of 2.85. This yields the field of view shown in Figure 28, with the size of an individual super-pixel footprint in the same scale also shown.

We now use a smaller subframe of our image of Cape Canaveral. The results of the image reconstruction process with a set of noiseless measurements are shown

in Figure 29. The reconstructed image contains all of the high-resolution features of the scene, particularly those of higher contrast. However, some low-contrast, high-resolution features are not clear, and there are artifacts that occur where the super-pixels meet.

The convergence is very similar to the previous results (Figure 22), since we have a similarly limited sampling of the Fourier space. Furthermore, each iteration takes significantly more time due to the extra set of integrals in equation (3.2); with the line search, each iteration took approximately 5 minutes compared to seconds in the previous astronomical reconstructions. However, we have always expected that this method would trade computational requirements for metrology/structural requirements, and this does little to change those results.

Beyond the use of compiled, optimized code, rather than a first-pass *MATLAB* script, there are a number of ways this could be improved. The first is to improve the convergence of the previous simplified case with the limited Fourier sampling rate, to improve the rate of convergence and allow the cost function to drop to arbitrarily low values, as in the case with full sampling. A second approach to improving convergence speed is to simplify equation (3.2) in such a way that it maintains physical meaning. Taking only the measurements within the primary hexagonal grid and using a hexagonal two-dimensional fast Fourier transform, or implementing a rectangular grid may also allow more efficient algorithms. This would depend on a demonstration that the approximation of a small, discrete grid was sufficiently accurate to capture the physical process. Finally, using a neural network techniques to find a sufficient empirical algorithm is another option. This work simply shows that the reconstruction of the image from this type of system is possible, and that only improved algorithms are required for practicality.

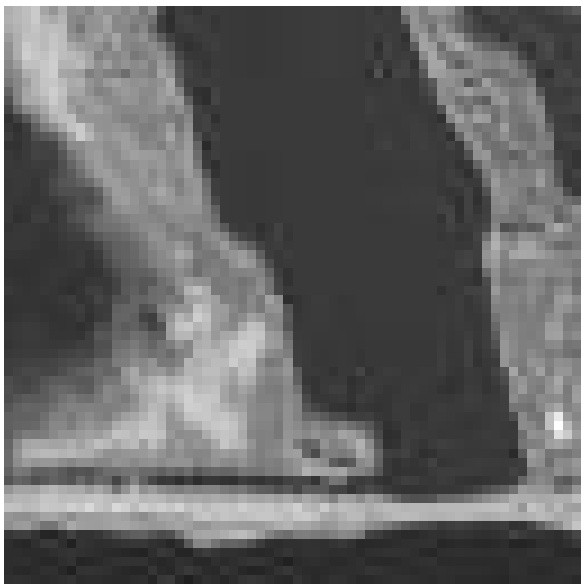

Original Image

Reconstructed Image

Fig. 29. Reconstructed image from simulated example TPD-ICI system

## E. Conclusion

The most important result of this work, the application of multiple super-pixels with transverse phase diversity, is the de-coupling of the swath width and the sub-aperture diameter, which mitigates many of the problems encountered when designing a successful ICI-based surface imaging system. For previous designs, which relied on a single super-pixel, swath-width requirements tended to drive the design to an unreasonably high number of very small apertures. This poses problems, both in increasing costs and signal quality. Because a large swath-width and sufficient context are critical for an earth-imaging system of any value, the application of TPD and multiple super-pixels is necessary for this kind of system.

TPD specifically eliminates concerns regarding translational and rotational ambiguities in the reconstructed image through the use of the known overlap. Although it is likely that intelligent routines would have been capable of using context clues to remove this problem, being able to eliminate them in a very robust manner is advantageous. However, the stricter requirements on optical quality and pointing precision that are necessary for imaging an extended scene remain.

The sparse sampling of the Fourier field does pose significant problems, specifically making the image reconstruction slow and difficult when compared to Fienup's original results. The conjugate gradient reconstruction method, while it does eventually reconstruct the image, never truly converges and instead continues to decrease by small increments; this result occurs both with a full simulation of the ICI system, and with the simplified case of a sparsely sampled transform. Further, because fewer measurements are taken, the resilience to noise is lower, and care must be taken to ensure that the problem is well-posed.

While this approach does show significant promise in making an ICI-based earth-

imaging system practical, work is still required to take full advantage of the method. Further development of the reconstruction algorithms to improve convergence are critical; these might involve simplifying the calculation of the estimated measurements, modifying the CG technique, using a second-order solver as we approach the solution, or applying neural network techniques. Also, the ability to detect and account for system state errors needs to be developed more fully.

# CHAPTER IV

## CONCLUSION

Intensity interferometry has long been neglected as an astronomical technique due to its low signal quality, loss of phase information, and general limitations. However, by expanding it beyond the original concept of a single baseline pair to an array of detectors, with new technology and advanced image reconstruction methods, the trades become more favorable. Initially, implementations of these methods were limited by the fact that any solution beyond the simplest system was highly non-linear and impossible to solve by hand. However, because of the exponential growth in computer technology in the intervening years, as well as improvements in sensing equipment, the original conclusions need to be re-examined. The ultimate idea is that in an age of ever-advancing computer technology, trading mechanical complexity for computational needs is an appealing proposition.

There are two ways we consider the use of ICI for observations: measurement of parameters and literal imaging. In measuring parameters, we define the scene in terms of its components, and estimate the measured mean-square mutual coherence, finding the parameters that minimize the variance between the actual and estimated measurements. In this way we translate the original phase retrieval problem to a non-linear programming problem for which there are many well-known solution techniques. While this is more generalized and robust than early ICI experiments, many forms of observation, such as detecting planetary systems and irregular features on distant stars are still extremely limited by the noise. The ultimate cause is that the signal quality drops off dramatically as the mutual coherence function does, and in many cases involve very large brightness variations. However, this does pose the possibility

of determining the configurations of bright but complex objects with an array of low-cost light collectors and detectors.

Obtaining a literal image is an expansion of the concept of parameter estimation: the parameters we wish to estimate are defined as the pixel intensity values within a known field of view. However, because the mean MCF decreases logarithmically as the size of the image increases, super-resolving the single ICI pixel by a factor of more than $\sim O(10)$, gives very poor signal quality, and thus extremely limits the swath width of a potential earth-looking system. However, by redesigning the focal plane apparatus to an array of multiple ICI pixels, each of which are super-resolved by a moderate amount, this limit is avoided, allowing a large, high-resolution image to be measured by a collection of smaller apertures without the extremely high precision requirements common to other sparse aperture techniques. Furthermore, the natural overlap of these super-pixels yields transverse phase diversity measurements, which can be used to improve the convergence of the system, eliminate ambiguities caused by the loss of the phase information, and generally make the system more robust.

While the nature of this thesis is theoretical, practical experiments are ongoing as well throught the GAIA testbed observatory. The details of this experimental setup are listed in the appendix.

Although we cannot eliminate the limitations of intensity interferometry, some of which are made clear in this work, there is still potential to use ICI devices to perform low-cost experiments, taking advantage of recent technological advancements, going far beyond the original Narrabri work. Future work enhancing and experimentally demonstrating these techniques have the potential to contribute to making large-baseline remote sensing more accessible.

# REFERENCES

[1] D. Eberly. (2004). Distance from a point to an ellipse in 2D. Geometric Tools. [Online]. Available:*http://www.geometrictools.com/*

[2] M. Born and E. Wolf, *Principles of Optics*, Cambridge: Cambridge University Press, 1997.

[3] P. R. Lawson, O. P. Lay, K. J. Johnston, C. A. Beichman, S. C. Unwin, et. al., "Terrestrial planet finder interferometer (TPF-I) whitepaper for the AAAC exoplanet task force," Tech. Rep., NASA Jet Propulsion Labs, Pasadena, California, April 2007.

[4] R. Hanbury Brown, R. C. Jennison, and M. K. Das Gupta, "Apparent angular sizes of discrete radio sources," *Nature, Lond.*, vol. 170, pp. 1061–3, 1952.

[5] R. Hanbury Brown and R. Q. Twiss, "A new type of interferometer for use in radio astronomy," *Phil. Mag.*, vol. 45, pp. 663–82, 1954.

[6] R. Hanbury Brown, J. Davis, and L. R. Allen, "The stellar interferometer at the Narrabri observatory - I," *Mon. Not. R. Astron. Soc.*, vol. 137, pp. 375–92, 1967.

[7] A. Ofir and E. N. Ribak, "Offline, multi-detector intensity interferometers I: Theory," *Mon. Not. R. Astron. Soc.*, vol. 368, pp. 1646–51, 2006.

[8] A. Ofir and E. N. Ribak, "Offline, multi-detector intensity interferometers II: Implications and applications," *Mon. Not. R. Astron. Soc.*, vol. 368, pp. 1651–6, 2006.

[9] V. Herrero, "Design of optical telescope arrays for intensity interferometry," *Astr. Journal*, vol. 76, pp. 198–201, 1971.

[10] I. I. Hussein, D. J. Scheeres, and D. C. Hyland, "Interferometric observatories in Earth orbit," *AIAA J. Guidance*, vol. 27, no. 2, pp. 297–301, 2003.

[11] D. C. Hyland, "Exo-planet detection via stellar intensity correlation interferometry," in *SPIE Conference Series*, Aug. 2005, vol. 5905, pp. 330–46.

[12] D. C. Hyland, "Entry pupil processing approaches for exo-planet imaging," in *SPIE Conference Series*, Aug. 2005, vol. 5905, pp. 219–37.

[13] J. W. Goodman, *Fourier Optics*, San Francisco: McGraw Hill, 1968.

[14] M. Golay, "Point arrays having compact, nonredundant autocorrelations," *J. Opt. Soc. Am.*, vol. 61, pp. 272–3, 1971.

[15] D. Hyland, "Calculation of signal-to-noise ratio for image formation using multispectral intensity correlation," in *Techniques and Instrumentation for Detection of Exoplanets III*, San Diego, California, Aug. 2007, pp. 6693–723.

[16] J. R. Fienup, "Reconstruction of an object from the modulus of its Fourier transform," *Opt. Letters*, vol. 3, pp. 27–9, 1978.

[17] The MathWorks, *Optimization Toolbox 4 Users Guide*, Natick, Massachusetts: The MathWorks, October 2008.

[18] R. H. Battin, *An Introduction to the Mathematics and Methods of Astrodynamics*, Reston, Virginia: AIAA, 1999.

[19] J. L. Crassidis and J. L. Junkins, *Optimal Estimation of Dynamic Systems*, New York, New York: Chapman & Hall/CRC, 2004.

[20] P. Foukal, "Stellar luminosity variations and global warming," *Science*, vol. 264, pp. 238–39, Apr. 1994.

[21] A. Ahad. (2004, Nov.). Magnitude of an exoplanet within the habitable zone. [Online]. Available: *http://www.astroscience.org/abdul-ahad/extrasolar-planets.htm*

[22] M. C. Chantell, D. Bhattacharya, C. E. Covault, M. Dragovan, R. Fernholz, et. al., "Prototype test results of the solar tower atmostpheric Cherenkov effect experiment (STACEE)," *ArXiv Astrophysics e-prints*, Apr. 1997.

[23] J. Grodecki and G. Dial, "IKONOS geometric accuracy," in *Joint Workshop of ISPRS Working Groups I/2, I/5 and IV/7 on High Resolution Mapping from Space 2001*, Hanover, Germany, Sept. 2001, pp. 1–10.

[24] M. Guizar-Sicairos and J. R. Fienup, "Image reconstruction by phase retrieval with transverse translation diversity," *Opt. Express*, vol. 16, pp. 7264–78, 2008.

[25] J. R. Shewchuk. (1994, Aug.). An introduction to the conjugate gradient method without the agonizing pain. Carnagie Mellon University. [Online]. Available: *http://citeseerx.ist.psu.edu/viewdoc/summary?doi=10.1.1.110.418*

[26] J. Goodman, C. Max et al., "Intensity interferometry," Associated report published by the MITRE Corporation through the JASON office, October 2008. Available: Request from National Reconnaissance Office

[27] Meade Instruments Corporation, *Instruction Manual: 16" LX200GPS Schmidt Cassegrain Telescope*, Irvine, California: Meade Instruments Corporation, October 2003.

[28] SBIG Astronomical Instruments, *ST-7XME and ST-7XMEI Enhanced QE CCD Cameras*, Santa Barbara, California: SBIG Astronomical Instruments, October 2008.

[29] SensL Inc., *SPMMini High Gain APD (Datasheet)*, Blackrock, Cork, Ireland: SensL Inc., September 2008.

[30] Inc. Optec, *Model TCF-S: Temperature Compensating Focuser Technical Manual*, Lowell, Michigan: Optec, Inc., January 2006.

[31] Inc. Optec, *Model IFW: Intelligent Filter Wheel Technical Manual*, Lowell, Michigan: Optec, Inc., August 2007.

# APPENDIX A

## DERIVATION OF THE VAN CITTERT-ZERNIKE THEOREM

The mutual coherence is a measure of the similarity of the electromagnetic field at two points in space. Defining the field at a point $k$ as $V_k$, the mutual coherence of the field between points $i$ and $j$ is

$$\Gamma_{i,j} = \langle V_i^* V_j \rangle \,. \tag{A.1}$$

Using the Huygens-Fresnel principle, and given a field in the image plane $U(\rho)$, the field in far plane is

$$V_k = V(\mathbf{r}_k) = \iint_S U(\rho) \frac{\exp[-ik|\rho - \mathbf{r}_k|]}{|\rho - \mathbf{r}_k|} d^2\rho. \tag{A.2}$$

Combining these two equations gives

$$\Gamma_{i,j} = \iint_S \iint_S \langle U^*(\rho_1) U(\rho_2) \rangle \, \frac{\exp[-ik(|\rho_1 - \mathbf{r}_i| - |\rho_2 - \mathbf{r}_j|)]}{|\rho_1 - \mathbf{r}_i| \cdot |\rho_2 - \mathbf{r}_j|} d^2\rho_1 d^2\rho_2. \tag{A.3}$$

At this point we make the assumption that each distinct source is incoherent with respect to the others, so that the only components that have an impact on the coherence measurements arrive at both detectors from the same source (i.e. $\rho_1 = \rho_2$). This allows us to reduce the previous equation to

$$\Gamma_{i,j} = \iint_S \langle I(\rho) \rangle \, \frac{\exp[-ik(|\rho - \mathbf{r}_i| - |\rho - \mathbf{r}_j|)]}{|\rho - \mathbf{r}_i| \cdot |\rho - \mathbf{r}_j|} d^2\rho. \tag{A.4}$$

Through some manipulation, the distances can be approximated as

$$|\rho - \mathbf{r}_k| = R - \frac{1}{R} \rho \cdot \mathbf{r_k} \tag{A.5}$$

where $R$ is the separation between the origins of the object and the imaging system, and the vectors $\mathbf{r}$ and $\rho$ are measured from their respective origins. Applying this approximation gives what is commonly known as the van Cittert-Zernike theorem

$$\Gamma_{i,j} = \frac{1}{R^2} \iint_S \langle I(\rho) \rangle \exp[-2\pi i(\mathbf{x} \cdot \rho)] d^2\rho, \tag{A.6}$$

so that the mutual coherence function is, within a reasonable approximation, the Fourier transform of the image intensity. Note that the Fourier coordinate vector $\mathbf{x} = \lambda^{-1}(\mathbf{r}_j - \mathbf{r}_i)$, so that the relative separation of the detectors, commonly called the *baseline*, is the relevant design parameter.

# APPENDIX B

## EXPERIMENTAL APPARATUS

The Giant Astronomical Interferometer Array (GAIA) at Texas A&M University serves as a testbed for ICI concepts. The current equipment consists of a two detector assemblies and a single baseline, but the methodology exists to expand the array to many more detectors, both locally and across the state of Texas. The project was started in 2006. This appendix will give details on the equipment, data collection methods, and initial measurements.

The initial GAIA array consists of two 16" telescopes, one fixed and one mobile, located at the Texas A&M Physics Teaching Observatory, near Easterwood Airport in College Station, Texas. The location is not ideal for astronomy, with poor seeing conditions caused by the low altitude and humid atmosphere, and significant light pollution from the airport and the city of College Station. However, the particulars of intensity correlation measurements mean that our experiments will be minimally impacted by the poor conditions. For an astronomical (i.e. non-resolvable) target, variations in the point spread function, such as those caused by atmospheric distortion, have little impact as long as stray light is prevented from impacting the detector too significantly, and the sensor is large enough on the focal plane to capture all of the light from the target. Because all of our targets will necessarily be very bright due to the signal to noise quality, light pollution is not as significant as it would be for more traditional work.

The telescopes are each 16" Meade LX200-GPS with altitude-azimuth motorized mounts, as pictured in Figure 30. The f/10 Schmidt-Cassegrain reflective design is compact and easy to manage, and has a total aperture area of 0.13 square meters [27].

Each telescope has two additional telescopes attached. The first situated above the instrument is the standard finder scope for the main telescope, and is used for coarse manual pointing. The second telescope, a 120mm Orion refracting telescope is fitted with an SBIG ST-7XME Deluxe CCD camera [28]. Because the main telescope will be fitted with the high-speed photodetector, this secondary telescope will be used for pointing control, allowing remote and automated control of the instrument.

The sensor is a SensL SPMMini1020 Avalanche Photodiode (APD) assembly, pictured in Figure 31. The instrument was selected for its robustness and simplicity. Silicon-based APDs are naturally more robust than photomultiplier tubes (PMT), the primary alternative: exposing an APD to high light levels simply saturates the output without the permanent damage that occurs in PMTs. The PMT is a more developed technology, with higher sensitivities and bandwidths, however, their fragility makes the APD a better choice for the initial work. The SMP package contains an on-board power supply and Peltier cooling equipment, and outputs a varying voltage signal through a BNC connection on the electronics board. The APD chip operates over all of the visible wavelength, peaking at 520 nanometers with a quantum efficiency of 14%. The frequency response drops to half of its initial magnitude at 10 MHz, approximating the limiting bandwidth of the device. The device is physically attached to the telescope by a C-mount adapter and standard 2" coupler. With a sensor diameter of 3 mm, the total length of focus for the f/10 scope is 3 centimeters, making focus control a minor concern [29].

A filter wheel and mechanized fine focuser connect the telescope and the sensor, pictured in Figure 32. While the length of the focus region is not as critical as in most other uses, the computer-controllable focus will allow an automatic maximization of the coherence that may improve the signal quality. The Optec TCF-S has a focus

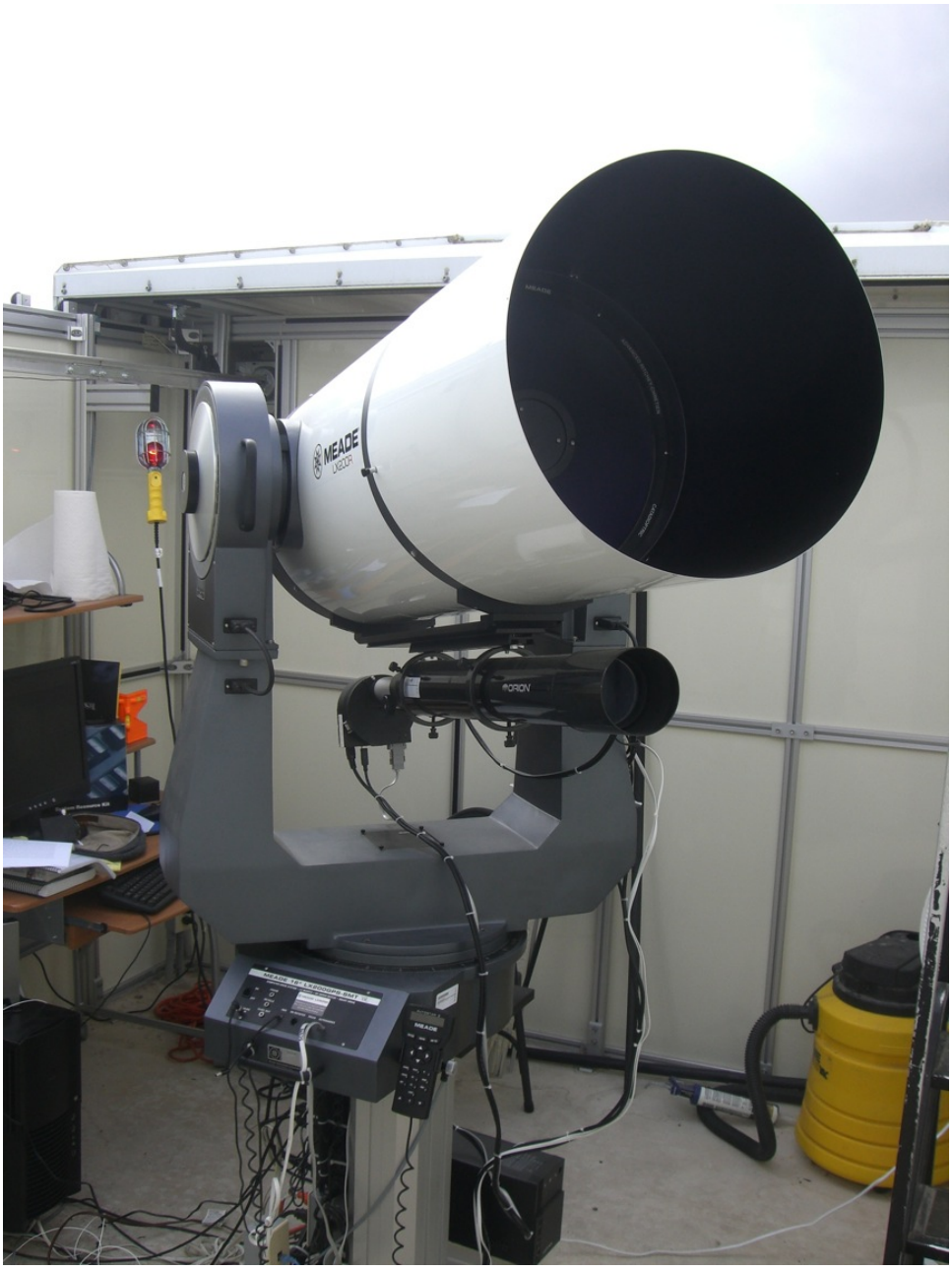


Fig. 30. Meade LX200-GPS telescopes used for GAIA experiment

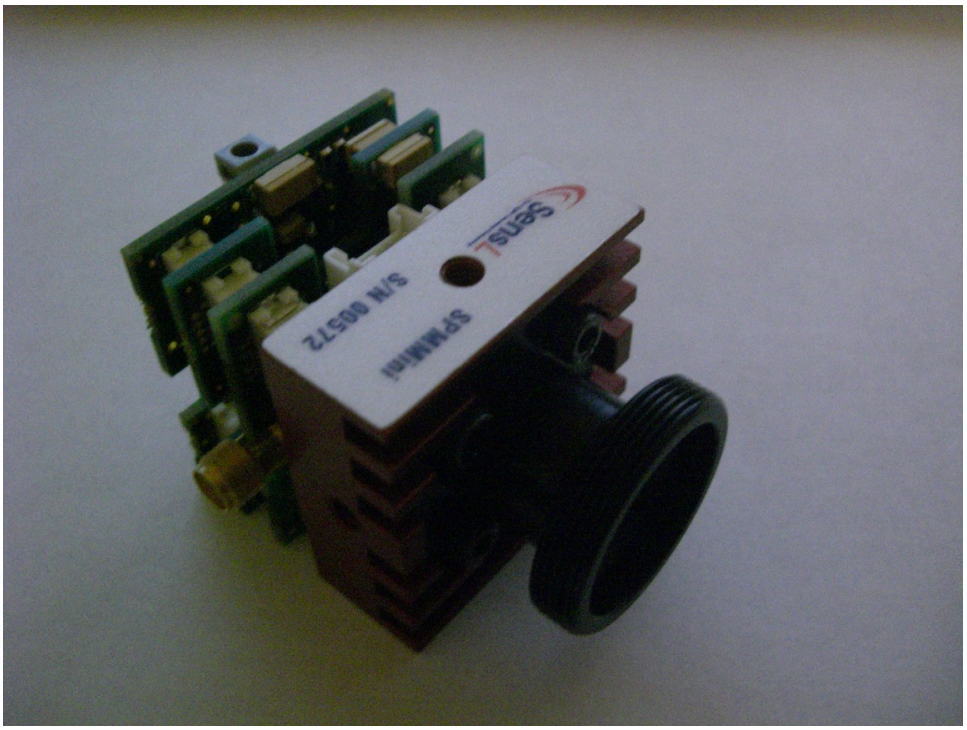


Fig. 31. SPMMini1020 avalanche photodiode assembly

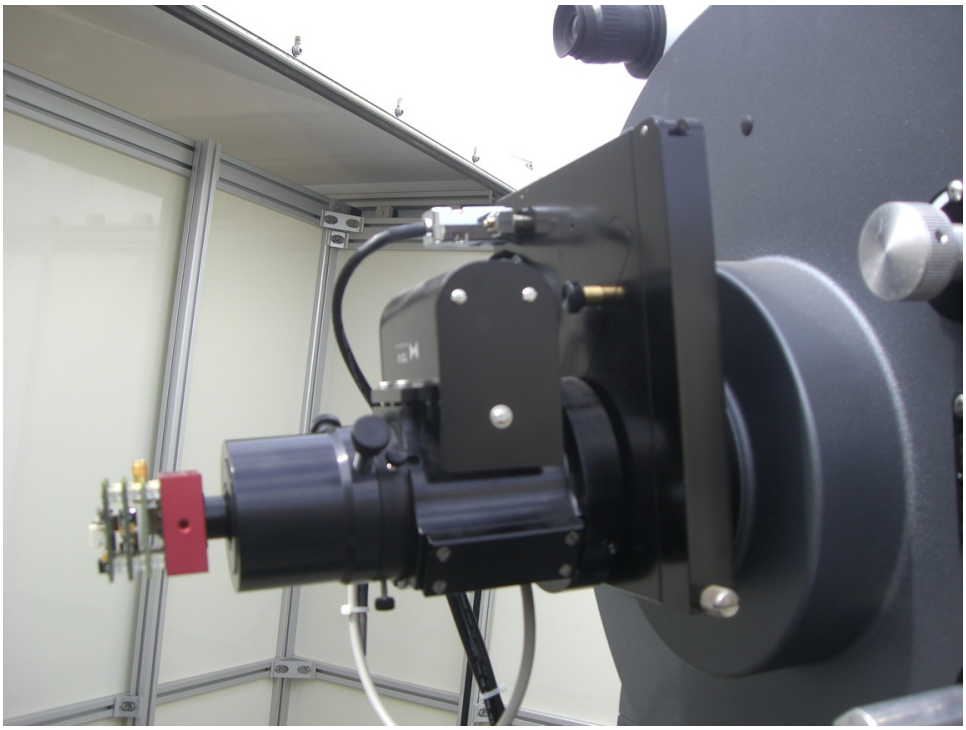

Fig. 32. Rear-mounted devices on the telescope

length of travel of 0.6", and automatically compensates for temperature fluctuations [30]. The Optec Intelligent Filter Wheel (IFW) serves two purposes. First, the development of ICI assumes a quasi-monochromatic light, implying a narrow wavelength band, which the filters provide. Second, recall that the Fourier position $(u, v)$ is proportional to both the relative positions *and* the the inverse of the wavelength. Thus, the availability of filters at multiple wavelengths also allows us to vary the baseline length without moving the physical detectors, improving the operational efficiency [31].

The fixed telescope is mounted in a standard Tele-Station 2 shelter, manufactured by Pier-tech Inc. It includes a retractable roof and an automatically elevating pier

Fig. 33. Pier-tech telescope shelter

mount, as shown in Figures 33 and 34. The shelter does not protect well against wind; on days with high winds, imaging can be difficult or impossible. However, the advantages of ICI again limit these problems, making this a good solution for our experiments. The roof and the pier can be controlled manually with a control panel on the wall; the control system also ensures that the pier is lowered before the roof closes, preventing accidental damage to the equipment. It can also be controlled through computer software provided by Pier-tech, allowing remote/automated control.

The mobile telescope is mounted on a prototype Star Traveller Mobile Observatory from Pier-tech, shown in Figure 35, similar in design to the fixed site, but with additional features. While the power for the fixed site is provided by campus

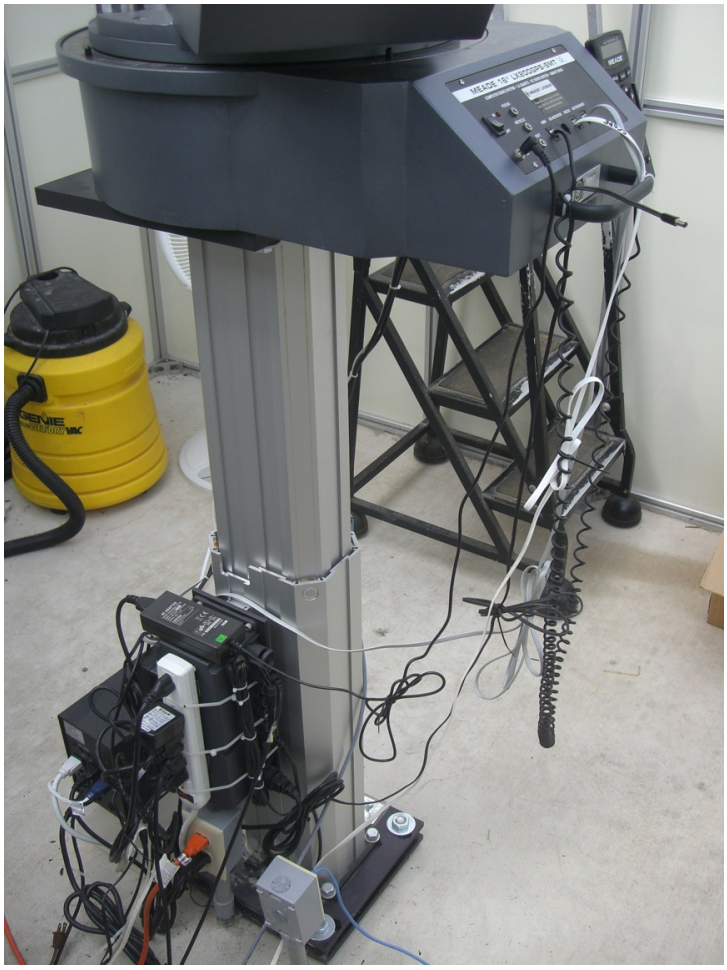

Fig. 34. Telescope raising pier

Fig. 35. Pier-tech mobile telescope shelter

utilities, power for the mobile unit is powered by a solar array mounted above the entrance, with large marine batteries used to sustain operation through the night (Figure 36). The pier itself is designed to be fixed to the trailer for travel, but can be placed directly on the ground to isolate it from trailer vibrations for observations, using the hydraulic jacks shown in Figure 37. The roof, pier and control system all operate similarly to their counterparts in the fixed station.

The control and data acquisition systems are run through a single AMD Athlon 64 X2-class PC for each detector. The telescope pointing, fine focuser, filter wheel, and shed control are all controlled through RS-232 serial ports, with access to the CCD camera over USB. *The Sky 6* and the *Automated Control Panel* (ACP) facilitate

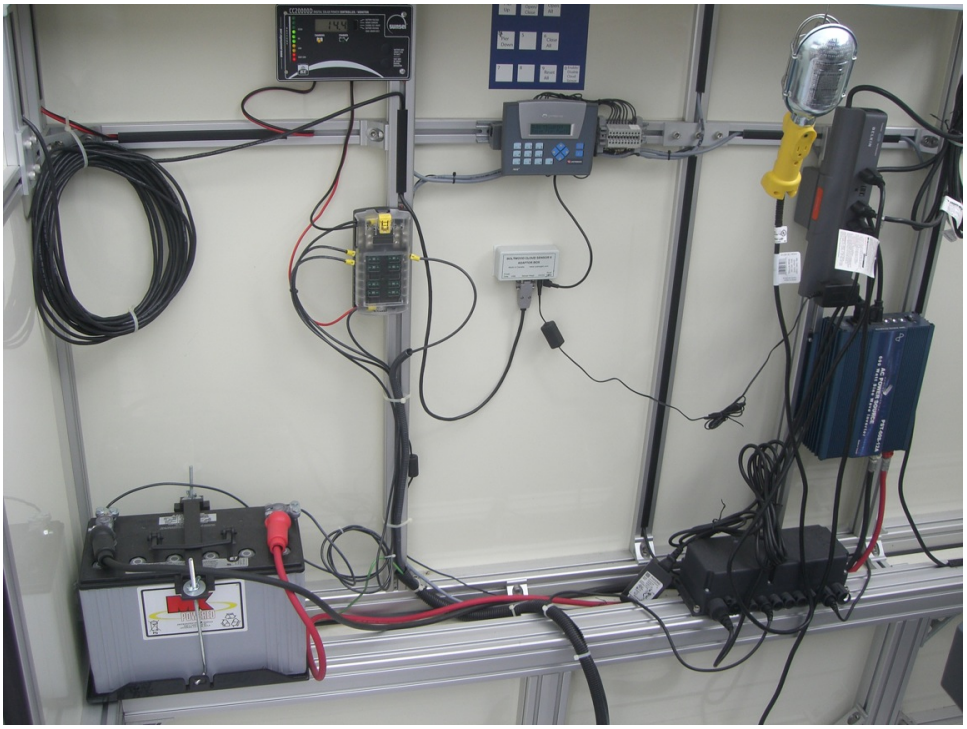

Fig. 36. Power systems for mobile observatory

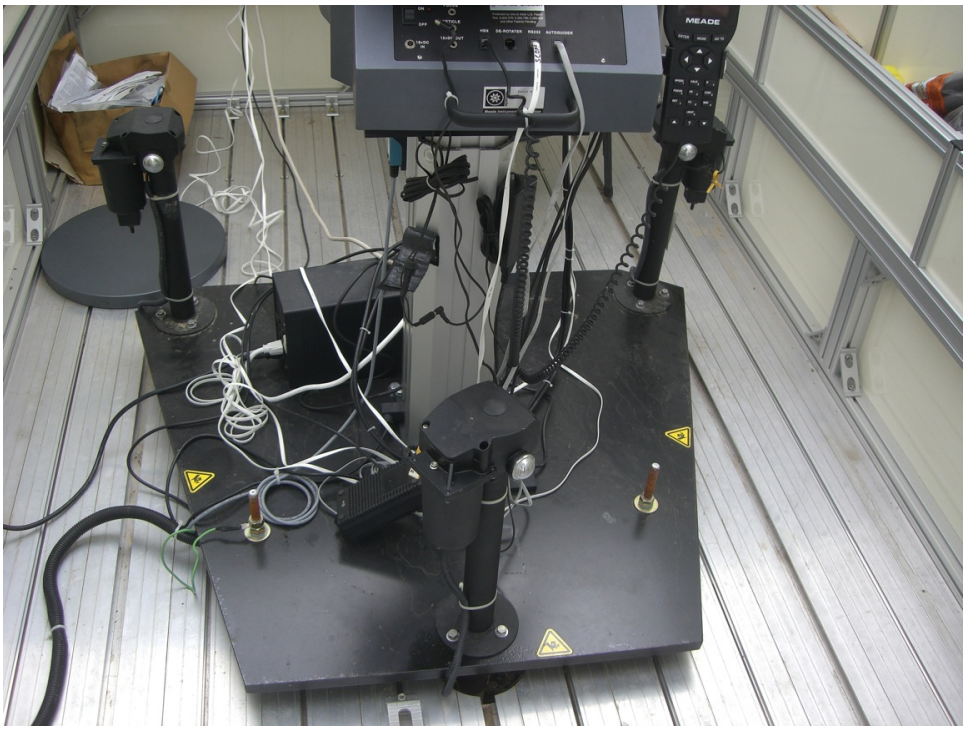


Fig. 37. Pier-tech mobile telescope pier isolated from the trailer

control of all the pertinent systems. The Microsoft Remote Desktop Protocol (RDP), allows remote operation of the observatory from any terminal on the TAMU network. Furthermore, the ACP Planner allows the user to create automated observation plans for the night. In order to do this, it was necessary to ensure that no cable-wrapping or accidental damage to equipment. Wireless 802.11 protocol networking is used to allow remote access and control of the mobile observatory.

Data acquisition from the APD assembly is handled by a National Instruments PCI-5114 high speed digitizer. The digitizer has a maximum sample rate of 250 MS/s (125 Mhz at the Nyquist limit), with 8-bit sampling on two channels. These cards are generally designed to read the very high speed data into onboard memory, and then write that information to the hard drive after the measurement. However, because the mode of operation for the ICI detector is to record data for a very long period of time, collecting hundreds of gigabytes of data over the entire night, the system must be customized to record directly to the hard drive. The PCI bus is limited to a data rate of 120 MB/s, and typical hard drives face similar limits, so that the maximum bandwidth the system is capable of for sustained measurement is 60 MHz, at the Nyquist limit with the 8-bit sample size. However, since the APD has a maximum bandwidth of approximately 10 MHz, this is sufficient for our purposes. The standard software for the digitizer does not operate in this manner however, so custom software based on the National Instruments API is necessary to capture the data.

In order to facilitate the actual correlation of the recorded data, the digitizers write directly to an external eSATA drive which can then be easily disconnected and moved to a common, high-power computer. The eSATA connection was chosen because it is as fast as the standard internal SATA protocol. Once connected to the same machine, each set of data will then have a digital high-pass filter applied. The

cross-correlation calculation must be handled more carefully, due to the variations in the timing between the two signals. This time difference $\tau$ has two sources. The first is physical, tied to the extra distance the light must travel to reach the second detector when looking at an off-zenith target, and can be calculated. The second is the difference in time-stamps between the two machines. Because the IP protocol is designed to be fault tolerant, it can not be depended on to provide very accurate time synchronization. In order to account for this, the value of $\tau$ can be varied on small portions of the data, attempting to maximize the coherence measurement. Doing this at multiple points will allow the time constant to be measured, including any variations over time.

# VITA

Brian Thomas Young received his Bachelor of Science degree in aerospace engineering from Texas A&M University in May 2007. His research interests are optimal control and estimation, design and control for large optical systems, and systems engineering of space systems.

Mr. Young will be taking a position as a navigation engineer at NASA/CalTech's Jet Propulsion Laboratory in Pasadena, California. He may be reached at H.R. Bright Building, Rm. 701, Ross Street - TAMU 3141, College Station TX 77843-3141. His email is btyoung@gmail.com.